Photocurrents from the Direct Irradiation of a Donor−Acceptor Complex Contained in a Thin Film on Indium Tin Oxide

4 AUTHORS, INCLUDING:

Scott Alan Trammell
United States Naval Research Laboratory
72 PUBLICATIONS **2,033** CITATIONS

Walter J Dressick
United States Naval Research Laboratory
113 PUBLICATIONS **3,317** CITATIONS

Martin H Moore
United States Naval Research Laboratory
**39** PUBLICATIONS **1,579** CITATIONS

Photocurrents from the Direct Irradiation of a Donor−Acceptor Complex Contained in a Thin Film on Indium Tin Oxide

Scott A. Trammell,* Walter J. Dressick, Brian J. Melde, and Martin Moore

Center for Bio/Molecular Science & Engineering, Naval Research Laboratory, Code 6900, 4555 Overlook Avenue, S.W., Washington, D.C. 20375, United States

S *Supporting Information*

ABSTRACT: We describe the performance of a photoelectrochemical cell based on an electron donor−acceptor (EDA) complex formed by the association of tetraphenylborate anion with a viologen dication siloxane film immobilized on an indium tin oxide (ITO) electrode. Visible irradiation of a weak absorbance band of the EDA complex leads to simultaneous photoreduction of the viologen and photooxidation of the tetraphenylborate, forming a viologen monocation radical and tetraphenylborate radical. Spontaneous decomposition of the latter to products incapable of further reaction inhibits reverse electron transfer, permitting harvesting of the redox equivalents stored as the viologen monocation radical at the electrode. Results of statistically designed two-level factorial experiments indicate that the photocurrent increases with light intensity (L) and viologen coverage (P), but decreases with viologen siloxane film age (A). Although the solution BPh_4^- concentration (F) does not significantly affect the photocurrent response under our experimental conditions, the nature of the electrolyte anion (C) does. Although significant interactions among the L, P, A, and C variables exist, our analyses provide a model that (1) describes the viologen film aging; (2) adequately predicts cell photocurrent responses as functions of levels of the L, P, and, to a somewhat lesser extent, A variables; and (3) identifies areas for improvement and optimization of cell performance.
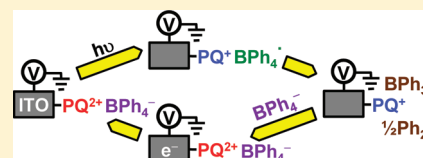
INTRODUCTION

Electron donor−acceptor (EDA) complexes are spontaneously formed as a result of thermodynamically favorable associations between electron-rich donor and electron-poor acceptor species. Their formation is typically accompanied by the appearance of a weak absorbance band associated with a transition involving the transfer of an electron from the donor to the acceptor component of the complex. In many cases, the energy of this electron-transfer transition corresponds to that of visible light frequencies, imparting a color to the complex. This ability to induce an electron-transfer event in such structurally simple systems makes EDA complexes popular as models for the study of electron-transfer processes[1−8] and provides a basis for their catalysis of a variety of chemical transformations.[9−14]

The donor−acceptor interaction has also been cleverly exploited for numerous applications, including the development of sensors;[15−22] molecular machines;[23] artificial muscles;[24] switches;[25] stimuli-responsive,[26] photochromic,[27] electrochromic,[28,29] self-healing,[30] controlled wettability,[31] chromatographic,[32] and heat-absorber[33] materials; organic electronic[34−37] and optoelectronic[38−41] devices; and, of course, solar cells.[42−46] With regard to the latter, economical conversion of light into electrical energy requires efficient initial transfer of an electron from the donor to the acceptor during irradiation, coupled with processes for separation of the resulting electron−hole pair (i.e., exciton) to harvest its stored energy that are competitive with its rapid thermal degradation through reverse electron transfer. Although significant progress has been made in this regard to understand and control the physicochemical,[47−50] interfacial,[51,52] and

morphological[52,53] properties of EDA complexes required to optimize performance, the goal of reproducibly fabricating an economically viable solar cell remains elusive.

Whereas direct conversion of solar energy entirely into electrical power is highly desirable, other options such as chemical storage of at least a portion of the energy are also attractive. In such photoelectrochemical cells, either or both the hole or/and electron can be used to drive chemical reactions at electrodes in which "sacrificial" reagents in solution are transformed into new and potentially useful species. The sacrificial reagent is ideally a cheap and abundant compound, such as water, and the new material is ideally a desirable compound, such as H_2, that stores a portion of the solar energy in the form of its enhanced chemical potential. A variety of simple photoelectrochemical cells of this type have been described in which a photosensitizer capable of strongly absorbing visible light participates in a spontaneous electron-transfer reaction with a quencher species, with the direction of electron transfer governed by the redox properties of the quencher and the photosensitizer excited state.[54−65]

For most such photoelectrochemical cells described to date, the photosensitizer excited state acts as a donor, transferring an electron to the acceptor quencher to generate an oxidized photosensitizer and reduced quencher pair.[55,58,60−65] The reverse electron-transfer reaction is inhibited by the sacrificial

reagent, which rapidly and (usually) irreversibly reacts with either, but not both, the oxidized photosensitizer or reduced quencher to regenerate the starting photosensitizer or quencher species, respectively. The species remaining in solution (i.e., reduced quencher or oxidized photosensitizer) is returned to its preirradiation oxidation state by reaction at an electrode, where its redox equivalents are converted to an external electric current that can be used to drive an appropriate redox reaction at an electrode in a second half-cell. For example, various alkylamine sacrificial reagents irreversibly react with oxidized photosensitizers to regenerate the photosensitizer and produce aldehyde products that do not typically react with the reduced quencher, which persists in solution and can be used to generate H_2 in a second half-cell.[58,65] The net reaction in such a photoelectrochemical cell is the photodecomposition of the alkylamine to produce aldehyde and H_2. Analogous photoelectrochemical cells have been described in which oxidized photosensitizer, rather than reduced quencher, persists in solution through use of acceptor quenchers that simultaneously function as sacrificial reagents[55,57,61−64] or dimerize to form two-electron redox species that inhibit the back-electron-transfer reaction with the singly oxidized photosensitizer.[62,66,67] In addition, examples of photoelectrochemical cells in which the photosensitizer excited state acts as an electron acceptor have also been described for the generation of species such as hydrogen peroxide[56] and bromine from oxygen and bromide ion, respectively.[54,59]

The simplest of these photoelectrochemical cells utilizes the EDA complex comprising the tetraphenylborate salt of methyl viologen, $MV^{2+}(BPh_4^-)_2$, as combined photosensitizer, quencher, and sacrificial reagent.[60] Irradiation of the EDA absorbance band of $MV^{2+}(BPh_4^-)_2$ in deaerated acetonitrile solution leads to electron transfer from the BPh_4^- donor to the MV^{2+} acceptor, followed by rapid irreversible decomposition of the $BPh_4^\bullet$ radical to triphenylboron and biphenyl. Redox equivalents stored in the reduced viologen cation radical formed, MV^+, are harvested at a Pt electrode to regenerate MV^{2+}.

However, similarly to its more complex brethren, the MV^{2+}-$(BPh_4^-)_2$ cell suffers disadvantages related to the solution environment. In particular, MV^+ generated in the solution must be transported by diffusion or convective mixing to the electrode surface, introducing a time lag between generation and harvesting of its redox equivalents. Because MV^+ exhibits strong absorbance in the visible light region that competes with absorbance due to the EDA complex, an inner filter effect leading to decreased cell efficiency occurs as the MV^+ concentration increases during the photolysis.

These issues have prompted us to consider modified versions of such simple photoelectrochemical cells in which the donor and/or acceptor components are confined at the electrode surface as a thin film. Confinement offers the opportunity to minimize complications such as inner filter effects because the redox equivalents carried by the reduced acceptor (or oxidized photosensitizer) can be immediately harvested to regenerate the quencher (or photosensitizer). In addition, the use of film architectures offers the possibility to position multiple donors and/or acceptors having appropriate redox properties within the film to enhance separation of the initially generated electron−hole pair, thereby further inhibiting the reverse electron-transfer reaction, and control the direction of electron transfer to improve cell efficiencies.

As a first step in this direction, we report here the results of our initial investigation of a photoelectrochemical cell based on viologen

Scheme 1. Chemical Structures and Abbreviations for Materials Described in the Text[a]
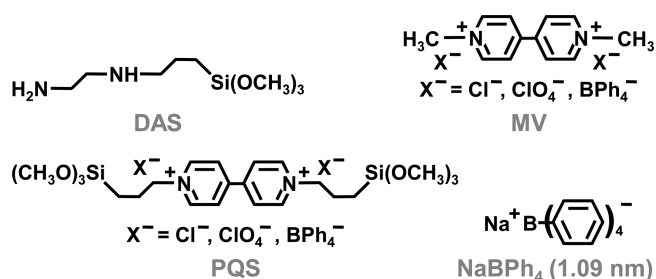
[a] Value in parentheses below the tetraphenylborate structure indicates its diameter, as determined from the geometric average from its X-ray crystal structure (see the Experimental Section).

films formed on indium tin oxide (ITO) electrode surfaces by electrochemically induced hydrolysis and chemisorption of a viologen silane precursor, PQS (see Scheme 1). The PQS films are characterized by a porous, open siloxane-bridged network[68−70] that permits ready access of BPh_4^-, leading to the formation of a photoactive tetraphenylborate−viologen EDA complex. Our cell therefore represents a film analogue of the acetonitrile-solution-based $MV^{2+}(BPh_4^-)_2$ photoelectrochemical cell described previously.[60] We statistically analyze the photocurrent response of the cell as functions of light intensity (L), viologen levels within the PQS film (P), PQS film age (A), solution levels of tetraphenylborate (F), and nature of the electrolyte anion (C) using a two-level factorial design. The analysis reveals significant interactions between the variables studied on the photocurrent response, which are interpreted in terms of a model consistent with confinement of the reagents within the film environment.

■ **EXPERIMENTAL SECTION**

1. Materials. Deionized water (18 MΩ·cm) for aqueous experiments was obtained from an Elix 5 Milli-Q Plus Ultra-Pure Water System (Millipore Corp.). All other materials were used as received from the indicated commercial source unless noted otherwise. Diethyl ether (>99%, laboratory grade, no. E134-4, lot no. 086899) and sodium nitrate ($NaNO_3$, >99%, certified ACS grade, no. S-343, lot no. 704666) were both from Fisher Scientific, sodium hexacyanoferrate(II) decahydrate [$Na_4Fe(CN)_6 \cdot 10H_2O$, no. 39660, lot no. I01U09] was from Alfa-Aesar, and sodium perchlorate ($NaClO_4$, ≥98%, anhydrous, reagent grade, no. 91, lot no. L504154) was from GFS Chemicals. Acetonitrile (99.8%, anhydrous Sure-seal, no. 271004, lot no. 40496KK), ethyl acetate (≥99.5%, ACS reagent grade, no. 319902, lot no. 46196HM), 3-N-morpholinopropanesulfonic acid (MOPS, 99.5%, no. M1254, lot no. 118K0055), sodium hydroxide (NaOH, 99.99%, semiconductor grade, no. 306576, lot no. 03720TN), sodium chloride (NaCl, 99.5%, Sigma Ultra, no. S7653, lot no. 036K0108), sodium tetraphenylborate ($NaBPh_4$, ≥99.5%, ACS reagent grade, no. T25402, lot no. 18220PI), ferrocenecarboxylic acid (CpFeCpCOOH, 97%, no. 10,688-7, lot no. 01430MI), glacial acetic acid (HOAc, >99.99%, no. 338826, lot no. 07808AY), dipotassium hydrogen phosphate (K_2HPO_4, 98%, anhydrous, no. P9791, lot no. 082K0008), and sodium bromide (NaBr, >99%, ACS reagent grade, no. 310506, lot no. 07713BC) were all obtained from Sigma-Aldrich Chemicals. 3-Iodopropyltrimethoxysilane (>95%, no. 58035, lot no.

0001419707; 79—80 °C, 2 mmHg) from Sigma-Aldrich Chemicals and N-(2-aminoethyl)-N-3-aminopropyltrimethoxysilane (DAS, no. SIA0591.0, lot no. 1 L-17609; 139—141 °C, 15 mmHg; see Scheme 1) from Gelest, Inc., were each vacuum distilled as indicated immediately prior to use. 4,4′-Dipyridyl (98%, no. 289426, lot no. 07728MD) from Sigma-Aldrich Chemicals was recrystallized from ethyl acetate.

4,4′-Bis(3-trimethoxylsilylpropyl)-bipyridinium iodide (PQS) was freshly prepared as required using a slight modification of the literature procedure:[71] Briefly, 1.0 g of 4,4′-dipyridyl was dissolved in 100 mL of dry acetonitrile under nitrogen. Four milliliters of 3-iodopropyltrimethoxysilane was added, and the mixture was refluxed for 3 days under a dry N_2 atmosphere. Solvent was then quickly removed by rotary evaporation. The reddish-orange PQS product was purified by dripping a solution of the product in a minimal volume of acetonitrile into a 10-fold stirred excess of cold diethyl ether. This reprecipitation process was repeated twice, and included solvent was then removed from the solid product on a vacuum line (100 μm Hg, 30 min) prior to use. Tris(2,2′-bipyridyl)ruthenium(II) diperchlorate [Ru(bpy)$_3$-(ClO$_4$)$_2$, where bpy = 2,2′-bipyridine] was synthesized as the chloride salt[72] and purified using an ion-exchange chromatography method described elsewhere[73] before metathesis to the perchlorate salt. Tetrasodium tris[1, 10-phenanthroline-4,7-(m, p-sulfonatophenyl)]ruthenate(II) hexahydrate [Na$_4$Ru(BPS)$_3$·6H$_2$O, where BPS = bathophenanthrolinedisulfonate],[74] cis-bis-(2,2′-bipyridyl)osmium(II) carbonyl chloride perchlorate [cis-(bpy)$_2$Os(CO)Cl(ClO$_4$)],[75] and tetrasodium tris(2,2′-bi-pyridine-4,4′-dicarboxalato)ruthenate(II) hexahydrate [Na$_4$Ru-(DCbpy)$_3$·6H$_2$O, where DCbpy = 4,4′-dicarboxy-2,2′-bipyridine][76−78] were prepared as previously described. The radii for the calculation of the diameters of the compounds NaBPh$_4$,[79] Na$_4$Fe(CN)$_6$,[80] Ru(bpy)$_3$ClO$_4$,[80] (bpy)$_2$Os(CO)Cl(ClO$_4$),[81] and CpFeCpCOOH[82] were taken as the geometric average of the maximum radial length and the two orthogonal radial lengths from X-ray crystal structure data. For Na$_4$Ru(BPS)$_3$ and Na$_4$Ru-(DCbpy)$_3$, radii were calculated from an energy-minimized structure determined using the ACD/3D Viewer in the ChemSketch program from Advanced Chemistry Development, Inc.

ITO slides (part no. CB-50IN-S111), each bearing an indium tin oxide coating (R_s = 5−15 Ω) on one side of a piece of Corning 1737F aluminosilicate glass of dimensions 75 mm × 25 mm × 1.1 mm, were purchased from Delta Technologies Limited, Stillwater, MN. The ITO slides were cleaned immediately prior to application of the PQS coating (vide infra) by immersion in concentrated H_2SO_4 for 30 min, followed by copious rinsing in deionized water and drying in a filtered N_2 gas stream taken from liquid N_2 boil-off. A polished fused-silica slide of dimensions 25 mm × 25 mm × 1 mm and quartz slides of dimensions 50 mm × 25 mm × 1 mm from Dell Optics, Orange, NJ, and Quartz Scientific Inc., Fairport Harbor, OH, respectively, were cleaned as described elsewhere.[83] The clean fused-silica slide and two of the quartz slides were then coated with a DAS siloxane self-assembled monolayer (SAM) film using the literature procedure.[84] The DAS-coated substrates were stored in sealed Flouroware containers until needed for experiments.

The remaining clean quartz slides were coated with a film of PQS by immersion into a pH 8.9 aqueous solution containing 100 mM K_2HPO_4 and 0.9 mM PQS at room temperature (22 ± 2 °C) for various times ranging from 30 min to 3 days. After removal from the treatment solution, each sample was rinsed by successive dipping twice each in water, 0.1 M NaCl (aq) solution,

and water and then dried in the filtered N_2 gas stream and stored in a loosely capped Coplin jar under ambient conditions (22 ± 2 °C, 45−55% relative humidity) until needed for experiments. UV−visible absorbance spectra were measured for each PQS-coated quartz slide using a Cary 5 double-beam spectrophotometer with a baseline acquired using the DAS-coated quartz slides as blanks.

2. Cyclic Voltammetry (CV). All CV measurements were performed using a three-electrode configuration with a model 440 electrochemical workstation (CH Instruments, Austin, TX) interfaced to a Gateway E-1200 personal computer for data acquisition and processing. An ITO working electrode, Pt wire counter electrode, and Ag/AgCl reference electrode (Cypress Inc.) were used in a one-compartment Teflon electrochemical quartz crystal microbalance (EQCM) cell (CH Instruments, Austin, TX, no. CHI127) that was securely mounted and reproducibly positioned using a chuck on a Mellis−Griot optical bench. In addition to the three ∼1-mm-diameter access holes already present in the lid of the Teflon EQCM cell, another ∼6-mm-diameter circular hole was added to modify the lid to allow light to reach the ITO electrode for the experiments. The ∼6-mm-diameter hole was positioned on the lid such that placement of the counter electrode, reference electrode, and degassing tube in the access holes did not block the light path.

The EQCM cell was prepared for electrochemical experiments as follows: An appropriate ITO working electrode was fitted with a butyl rubber O-ring and placed in the bottom section of the Teflon cell, which was then screwed onto the body of the cell to provide a water-tight seal. The assembled cell was next secured to the optical bench using the chuck. The portion of the ITO electrode protruding from the cell assembly was connected to the potentiostat as the working electrode using an alligator clip. An aliquot of the solution to be studied was placed in the cell to equilibrate with the ITO electrode for ∼5 min. The solution was then discarded, and a fresh aliquot (∼3 mL) of the same solution was placed in the cell, which was then capped with the Teflon lid. The area of the ITO electrode exposed to the solution was 0.505 cm^2. The Pt wire counter electrode and the Ag/AgCl reference electrode were connected to the potentiostat and placed in the access holes in the lid, together with a Teflon tube serially connected to a gas bubbler containing the solution solvent and then to an Ar gas source. The ∼6-mm-diameter hole in the Teflon lid was covered with the DAS-coated fused silica slide, and the solution was bubble-degassed using solvent-saturated Ar for ∼10 min. The degassing tube was then gently lifted above the solution surface to maintain a blanket of Ar over the quiescent solution prior to acquisition of the cyclic voltammogram. All cyclic voltammograms were plotted according to the IUPAC convention, in which positive potentials are plotted in the positive x direction and anodic currents are positive.

3. Electrode PQS Modification. The Teflon EQCM cell was prepared as described in the preceding section using a clean ITO electrode. A solution containing 200 mM NaCl and 100 mM K_2HPO_4 at pH 8.9 with 0.9 mM PQS was added and Ar bubble-degassed. Cyclic voltammograms were then recorded in the quiescent solution under Ar atmosphere at a 100 mV/s scan rate in the potential window spanning from 0.0 to −0.8 V versus Ag/AgCl. Electrochemically facilitated hydrolysis of the PQS during the scans led to deposition of a cross-linked PQS siloxane film covalently bound to the ITO electrode, as previously observed.[68] The number of scans was varied to control the amount of electrochemically active PQ^{2+} deposited on the

surface of the ITO. The PQS film surface coverage was estimated from the total charge passed, as determined by integration of the voltammogram, for a completed film using the known reaction stoichiometry (i.e., one-electron reduction: $PQ^{2+} + e^- \leftrightarrow PQ^+$). After completion of the PQS film deposition, each ITO electrode was triply rinsed in water and then soaked for ~5 min in 0.1 M NaCl(aq) solution to completely exchange I^- and HPO_4^{2-} counterions for Cl^- counterions in the film. The PQS-coated ITO electrodes were then triply rinsed in water to remove excess NaCl, dried in the filtered N_2 gas stream, and stored in a loosely capped Coplin jar under ambient conditions (i.e., 22 ± 2 °C, 45–55% relative humidity) until needed for experiments.

4. Photolysis Conditions. The PQS-coated ITO electrodes were irradiated using an Oriel model 66001 UV–visible high-intensity 150-W Xe lamp assembly mounted to the optical table. The lamp assembly was positioned such that the light output was directed vertically onto the Teflon cell from a position ~90 cm above the ITO electrode. The light output reaching the ITO electrode was wavelength-filtered using an Oriel (no. 59482) 435-nm long-pass filter and moderated in intensity, where required, using 50% or 25% transmission neutral-density filters mounted to the lamp assembly. The lamp was operated at 145 W using an Oriel model 68805 universal power supply equipped with a model 68850 photofeedback controller that was maintained at a level of 3.72 ± 0.01 during lamp operation to provide maximum light output with minimal intensity variation during the experiments. An Oriel model 76995 electronic shutter was used to control exposure of the ITO electrode to the light. The photon fluence of the light delivered at the ITO electrode was measured at the electrode using Reineckate salt actinometry.[85] Because the tetraphenylborate–viologen EDA complex in the PQS film does not absorb light at $\lambda > 475$ nm (vide infra), light intensity measurements corresponding to its absorbance band position were made by difference, using Oriel no. 59482 435-nm long-pass and no. 51290 475-nm long-pass filters to successively bracket and determine the lamp output in the 435 nm < λ < 475 nm wavelength region.

5. Photocurrent Measurements. For a typical photocurrent measurement, the Teflon cell containing the appropriate PQS-coated ITO electrode, together with the Pt wire counter electrode and Ag/AgCl reference electrode, was assembled on the optical bench as described in section 2. Fluorescent room lights were extinguished, and the solution to be examined was placed into the cell and allowed to equilibrate with the ITO electrode for ~5 min before being discarded and replaced by a fresh aliquot of the same solution. All solutions were buffered at pH 7 with 1 mM MOPS and contained either 100 mM NaCl or NaClO$_4$ to maintain the ionic strength, as well as the amount of NaBPh$_4$ (i.e., 0–1 mM) required for the experiment. For some experiments, however, 100 mM NaBr or NaNO$_3$ was instead used to maintain ionic strength as discussed later in the text. All solutions were stored in the dark between uses to avoid any extended UV photolysis of the NaBPh$_4$. In all cases, background photocurrent (i_B) measurements were made for NaBPh$_4$-free blank solutions prior to photocurrent measurements of the corresponding NaBPh$_4$ solutions (i_P) under identical exposure conditions. The average net photocurrent due to photolysis of the BPh$_4^-$ (i_N) is reported as the difference of the average i_P and i_B, $i_P - i_B$.

To make a photocurrent measurement, the EQCM cell containing the appropriate solution was capped with the DAS-coated fused silica slide, and the solution was Ar-bubble-degassed for 10 min. The UV lamp assembly was fitted with the 435-nm

long-pass filter, as well as any neutral-density filter required to control the light intensity. The degassing tube was removed from the solution and positioned to maintain an Ar blanket within the cell during the measurement. The ITO electrode was set to a potential of −0.05 V versus the Ag/AgCl reference electrode, and the current was allowed to stabilize for ~1 min. This potential was chosen because (1) it was sufficiently far removed from the PQ$^{2+/+}$ redox waves for surface-bound PQS (i.e., $E_{1/2} = -0.52$ V) to ensure rapid, quantitative capture of the electron transferred to the PQ^{2+} from the BPh$_4^-$ during photolysis and (2) it represented the potential at which the maximum i_N value was observed in our experiments, as measured by the photocurrent difference $i_P - i_B$.

Once a stable dark current had been obtained, the electronic shutter was opened 5 s to irradiate the sample and then closed for 5 s to allow the current to return to its dark state, with the cycle repeated three times to acquire the data. The electrodes were then disconnected from the potentiostat, and the Teflon cell was removed from the optical bench and disassembled. The cell, the Pt wire counter electrode, and the Ag/AgCl reference electrode were triply rinsed in water and gently blotted dry with a lint-free tissue for immediate use in the next experiment. The ITO electrode was triply rinsed in water, gently blown dry in the N_2 gas stream, and stored in a loosely capped Coplin jar under ambient conditions (i.e., 22 ± 2 °C, 45–55% relative humidity) until needed again. The procedure described here was repeated using different experimental conditions dictated by the factorial design described in the next section until all 32 average i_N values required for the analysis matrix were obtained.

6. Factorial Design Experiments. The set of i_N values obtained were analyzed using the two-level factorial statistical design method described elsewhere.[86−88] Briefly, the variables examined here were electrode coverage of PQ^{2+} viologen in the PQS films (P), light intensity in the 435 nm < λ < 475 nm wavelength region (L), solution concentration of the BPh$_4^-$ reagent (F), age of the PQS electrode (A), and nature of the electrolyte anion (C). For each variable, high and low levels were selected for study and linearly coded as +1 and −1 values, respectively. Coded values for any experimental condition in which the magnitude of a variable was intermediate between its selected high and low levels were obtained by linearly mapping the magnitude onto the −1 to +1 variable range using the equation[87]

$$x = 2(q - a)/(b - a) - 1 \qquad (1)$$

In eq 1, a and b represent the low and high values for a given variable associated with its −1 and +1 values, respectively, in the factorial design; q is an intermediate value for the variable within the range $a \leq q \leq b$; and x is its corresponding value linearly mapped onto the $-1 \leq x \leq +1$ range.

A standard order design matrix comprising the $2^5 = 32$ possible combinations of the variable levels was prepared, for which (1) each row of the matrix specified a ±1 level for each variable, together comprising a set of conditions describing a particular experiment, and (2) the +1 entries in each row identified the variable or combination of variables associated with the effect derived from that experiment. The experiments described by each row were performed in random order to obtain the i_N value corresponding to each set of experimental conditions. The i_N values were then statistically analyzed using Yates' algorithm to determine the effect due to each variable and combination of
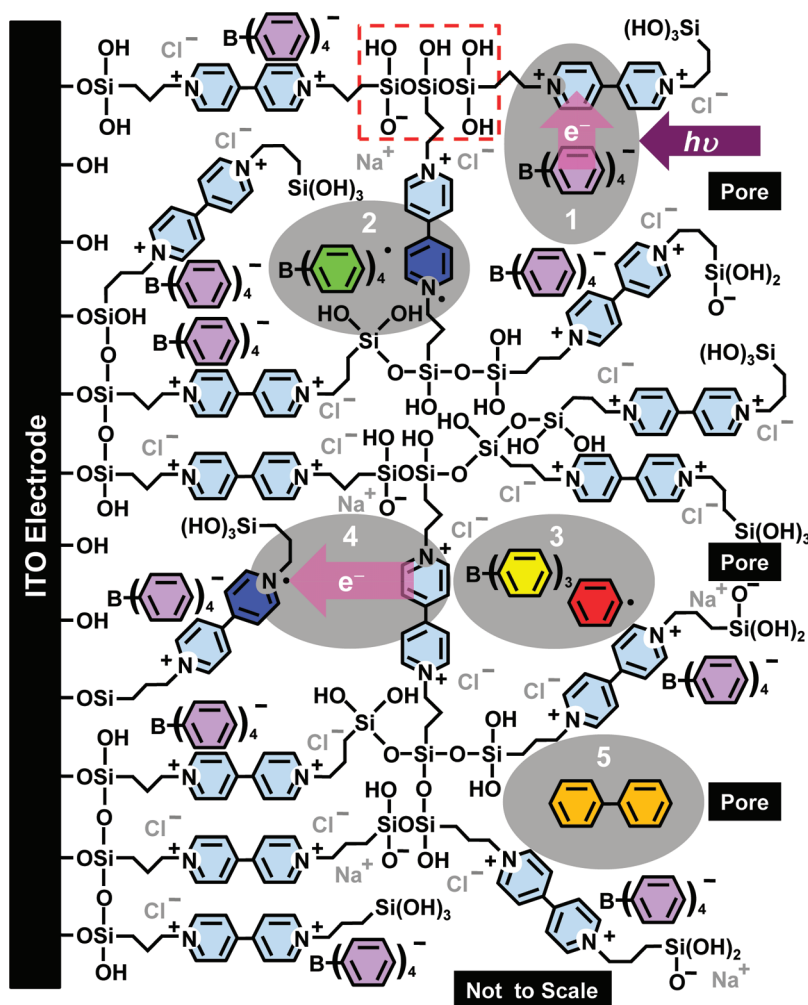
Figure 1. Cross-sectional schematic of the PQS film electrode on ITO. The PQ^{2+} species, tetraphenylborate anion, and PQ^+ monocation radical are shown in pale blue, purple, and dark blue color, respectively. Photolysis intermediates and products shown include the tetraphenylborate radical (green), triphenylboron (yellow), phenyl radical (red), and biphenyl (orange). The photolysis reactions are summarized in the labeled gray ellipses, as described in the text. The dashed red box identifies a cross-linking siloxane structure.

variables. Analysis of variance (ANOVA) was then applied to distinguish statistically significant, or real, effects from effects corresponding to random experimental error at the 99.9% confidence limit. Elimination of the latter resulted in a model describing the behavior of the i_N values as a function of the variables exhibiting real effects over the ranges of the variables studied, forming a basis for the discussion and understanding of the system presented in the remainder of the text. Further details concerning the calculations underlying our analyses are presented in the Supporting Information.

■ RESULTS AND DISCUSSION

An idealized cross-sectional view of the electrode half-cell studied here is shown in Figure 1. The electrodes comprise siloxane-cross-linked electroactive viologen (PQ^{2+}) species covalently bound to an ITO substrate, prepared by electrochemically accelerated hydrolysis of the PQS precursor of the structure shown in Scheme 1.[68] Figure 2A illustrates the deposition of the covalently bound PQS surface film as the ITO electrode potential is repeatedly cycled through the PQS solution $PQ^{2+/+}$ redox potential at $E_{1/2} = -0.67$ V, as shown by the

appearance and growth of cathodic and anodic current peaks having $E_{1/2} = -0.52$ V. Cyclic voltammograms for surface-immobilized PQS films exhibiting two different surface coverages are shown in Figure 2B in fresh aqueous pH 7 electrolyte buffer solution after completion of the deposition process. The separation of the anodic $(E_{p,a})$ and cathodic $(E_{p,c})$ current peaks clearly increases with film coverage, and there is no degradation of the current during repeated potential scans of these films. In addition, the amounts of charge passed are identical for the anodic and cathodic waves in each case, as measured by integration of the currents associated with each wave. These results indicate that our films exhibit chemically reversible behavior in which charge hopping through the electroactive PQ^{2+} groups represents the mechanism for electron transfer through the film.[69,89,90]

Immersion of a PQS film into an aqueous solution containing $NaBPh_4$ promotes exchange of the chloride or perchlorate anions associated with the PQ^{2+} sites by the more hydrophobic BPh_4^- species, consistent with previous studies of ion exchange[70] and the relative size of the BPh_4^- anion (see Scheme 1) and film pore size. For electrochemically deposited sol—gel-derived silicate films based on tetramethoxysilane, film pore sizes have been reported between 0.20 and 0.80 nm.[91] From electrochemical

13450

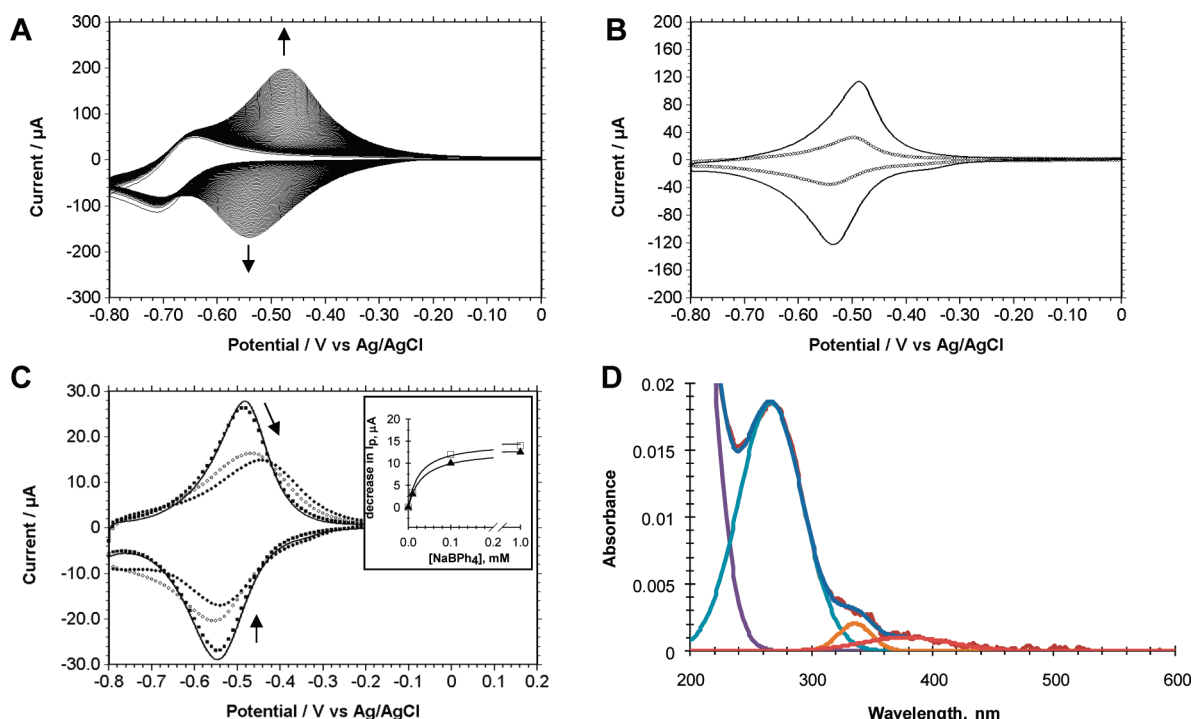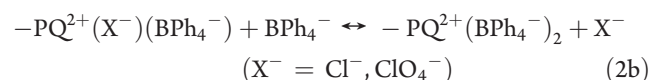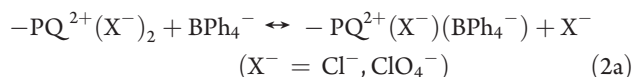dx.doi.org/10.1021/jp2023988 |*J. Phys. Chem. C* 2011, 115, 13446–13461

Figure 2. (A) Cyclic voltammograms of the growth of a PQ^{2+} siloxane film at an ITO electrode exposed to a buffer (200 mM NaCl and 100 mM potassium phosphate at pH 8.9) containing 900 μM PQS (diiodide salt) recorded under a blanket of Ar. Scan rate = 100 mV/s, number of scans = 68. (B) Cyclic voltammograms of two PQS siloxane films on an ITO electrode recorded in fresh Ar-deaerated buffer with no added PQS silane in solution. Scan rate = 100 mV/s. (C) Cyclic voltammogram of the PQS electrode (solid line) in electrolyte solution containing 100 mM NaCl and 1 mM MOPs at pH 7 with the addition of 0.01 mM (solid squares), 0.1 mM (open diamonds), and 1 mM $NaBPh_4$ (solid diamonds). Scan rate = 20 mV/s. Inset: Average of the anodic and cathodic peak currents measured from the cyclic voltammograms as a function of added $NaBPh_4$ in the range $0 \le [NaBPh_4] \le 1$ mM in solutions containing NaCl (open squares) and $NaClO_4$ (solid triangles) as the supporting electrolyte. (D) UV−visible absorbance spectrum of a PQS film chemisorbed for 4 h onto a quartz slide (see the Experimental Section) versus a DAS-coated quartz slide as a blank after exposure to 1 mM $NaBPh_4$. The deconvoluted strong absorbance band at ∼280 nm (∼340-nm shoulder) is characteristic of the PQ^{2+} species in our PQS film, and the weak absorbance band at ∼378 nm is attributed to the $(PQ^{2+})(BPh_4{}^-)(Cl^-)$ EDA complex.

probe experiments (see Figure S-1 and Table S-1, Supporting Information), we estimated the size of the pores for our PQS films as between 1.3 and 2.1 nm.

Ion exchange within the PQS film can, in principle, lead to formation of separate species in which the $-PQ^{2+}$ surface sites are singly or doubly ion paired by $BPh_4{}^-$, as shown in Figure 1 and eqs 2a and 2b

$$-PQ^{2+}(X^-)_2 + BPh_4{}^- \leftrightarrow -PQ^{2+}(X^-)(BPh_4{}^-) + X^-$$
$$(X^- = Cl^-, ClO_4{}^-) \tag{2a}$$

$$-PQ^{2+}(X^-)(BPh_4{}^-) + BPh_4{}^- \leftrightarrow -PQ^{2+}(BPh_4{}^-)_2 + X^-$$
$$(X^- = Cl^-, ClO_4{}^-) \tag{2b}$$

Given steric constraints and ion pairing of $BPh_4{}^-$ with the PQ^{2+} sites, variations in electron-transfer processes leading to unique $E_{1/2}$ values for $PQ^{2+}(X^-)_2$, $PQ^{2+}(X^-)(BPh_4{}^-)$, and PQ^{2+}-$(BPh_4{}^-)_2$ species within the PQS film might be expected. The cyclic voltammogram is, in fact, distorted in the presence of $BPh_4{}^-$, as shown in Figure 2C, with an increase in the separation of the cathodic and anodic peaks and a shift in the potential of the $PQ^{2+/+}$ redox couple. With increased addition of $BPh_4{}^-$, the resulting cyclic voltammograms reveal not two but rather only one new component with $E_{1/2} = -0.49$ V in the PQS electrode film with the bound $BPh_4{}^-$ anion. The anodic shift of ∼0.03 V in $E_{1/2}$ observed in the presence of $BPh_4{}^-$ anion indicates that ion

pairing between the PQ^{2+} sites and $BPh_4{}^-$ anion within the PQS film, whatever the ion-pair structure, clearly lowers the energy of the lowest unoccupied molecular orbital (LUMO) of PQ^{2+} in the film, facilitating its reduction.

The observation of a single new component with $E_{1/2} = -0.49$ V in Figure 2C suggests that either both the $PQ^{2+}(X^-)(BPh_4{}^-)$ and $PQ^{2+}(BPh_4{}^-)_2$ species fortuitously exhibit the same $E_{1/2}$ value or one predominates inside the PQS film. The first option seems unlikely, given simple electrostatic arguments and the sizable ∼0.03 V anodic shift observed for the $E_{1/2}$ value of the $PQ^{2+/+}$ redox process in the presence of $BPh_4{}^-$. In contrast, electrostatic and steric constraints within the PQS film should favor formation of smaller ion pairs, suggesting that $PQ^{2+}(X^-)$-$(BPh_4{}^-)$ will predominate. If we tentatively assign the $E_{1/2} = -0.49$ V component to the $PQ^{2+/+}$ redox process associated with the $-PQ^{2+}(X^-)(BPh_4{}^-)$ species, then the strength of the binding interaction between PQ^{2+} and $BPh_4{}^-$ in $-PQ^{2+}(X^-)(BPh_4{}^-)$ can be defined in eq 3 as a simple Langmuir binding curve.[92]

$$\theta_{PQ^{2+}(X^-)(BPh_4{}^-)} = \Gamma_{PQ^{2+}(X^-)(BPh_4{}^-)}/\Gamma_{total\,PQ^{2+}\,sites}$$

$$= K_X[NaBPh_4]/(1 + K_X[NaBPh_4]) \tag{3}$$

In eq 3, $\theta_{PQ^{2+}(X^-)(BPh_4{}^-)}$ is the fraction of $-PQ^{2+}(X^-)$ $(BPh_4{}^-)$ bound compared to the total number of $-PQ^{2+}$ sites, $\Gamma_{PQ^{2+}(X^-)(BPh_4{}^-)}$ is the surface coverage of the $-PQ^{2+}(X^-)(BPh_4{}^-)$,

$\Gamma_{\text{total PQ}^{2+}\text{ sites}}$ is the total surface coverage of PQ^{2+}, and K_X is the equilibrium constant for the formation of $-PQ^{2+}(X^-)(BPh_4^-)$.

By fitting the change in peak current as a function of $[NaBPh_4]$ (i.e., $\theta_{PQ^{2+}(X^-)(BPh_4^-)} = \Delta I_{p([NaBPh_4])}/\Delta I_{p(max)}$) to the competitive binding curve, we estimated K_X (see Figure 2C, inset). We found $K_{\text{chloride}} = 38000\ M^{-1}$ and $K_{\text{perchlorate}} = 31000\ M^{-1}$, indicating that the nature of the counterion displaced by BPh_4^- influences the equilibrium composition of the PQS film to a small extent.

Additional evidence supporting the predominance of one of the ion-paired species shown in eqs 2a and 2b within the PQS film is shown in the film absorbance spectrum of Figure 2D. In the absence of BPh_4^-, the absorbance spectrum of our PQS film is dominated by a band at ~280 nm (with a weaker shoulder at ~340 nm) associated with population of the PQ^{2+} $\pi-\pi^*$ excited state. However, a low-energy weak absorbance tail appears on this band after addition of BPh_4^-, which comprises a single component with an absorbance maximum at 378 nm consistent with our observation of a single electrochemical component at $E_{1/2} = -0.49$ V for PQS films exposed to BPh_4^-. Analogous behavior was observed elsewhere for the orange-yellow precipitate formed by mixing aqueous solutions containing methylviologen (MV^{2+}, see Scheme 1) and tetraphenylborate.[60] In that case, however, dissolution of the precipitate in acetonitrile revealed a somewhat broader absorbance tail, consistent with the presence of both $MV^{2+}(X^-)(BPh_4^-)$ and $MV^{2+}(BPh_4^-)_2$ species formed during reagent mixing in the unconstrained solution environment.

An extinction coefficient of $\varepsilon_{378} \leq 1.6 \times 10^6$ cm$^2\cdot$mol^{-1} was estimated for the BPh_4^- [highest occupied molecular orbital (HOMO)] $\rightarrow$ PQ^{2+} (LUMO) charge-transfer transition from the broad band centered at 378 nm in Figure 2D, assuming replacement of the X^- by BPh_4^- to form $PQ^{2+}(X^-)(BPh_4^-)$, by comparison with the PQ^{2+} $\pi-\pi^*$ absorbance at 281 nm ($\varepsilon_{281} = 3 \times 10^7$ cm$^2\cdot$mol^{-1}).[69] Extinction coefficients of this magnitude are typically associated with photoinduced electron-transfer transitions within EDA complexes, such as those observed for the analogous $MV^{2+}(BPh_4^-)_2$ species forming the basis of a previously described photoelectrochemical cell.[60] In fact, irradiation of the PQS electrode of Figure 1 at $\lambda \geq 435$ nm in an Ar-degassed solution containing BPh_4^- at a potential sufficient to oxidize any PQ^+ formed (e.g., -0.05 V versus Ag/AgCl) also results in production of photocurrent, as shown in Figure 3. By analogy with the corresponding solution-phase photoelectrochemical cell based on the $MV^{2+}(BPh_4^-)_2$ species,[60] photoinduced electron transfer from BPh_4^- to PQ^{2+} sites, as shown in the gray ovals labeled 1 and 2 in Figure 1 and in eq 4, must initiate the cell photoelectrochemistry

$$[PQ^{2+}(X^-)(BPh_4^-)] + h\nu \rightarrow [PQ^+(X^-)(BPh_4^\bullet)] \quad (4)$$
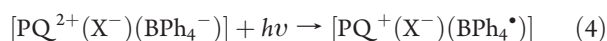
Given our previous observations and arguments indicating that the $PQ^{2+}(X^-)(BPh_4^-)$ species likely predominates within the PQS films, for simplicity during the remaining discussion, we neglect explicit contributions from any $PQ^{2+}(BPh_4^-)_2$ species present.

Because of the instability of the $BPh_4^\bullet$ radical,[93] there are two possible fates for the $[PQ^+(X^-)(BPh_4^\bullet)]$ excited state formed in eq 4. First, thermal deactivation by rapid reverse electron transfer can occur to regenerate the ground-state species through the reaction

$$[PQ^+(X^-)(BPh_4^\bullet)] \rightarrow [PQ^{2+}(X^-)(BPh_4^-)] \quad (5)$$
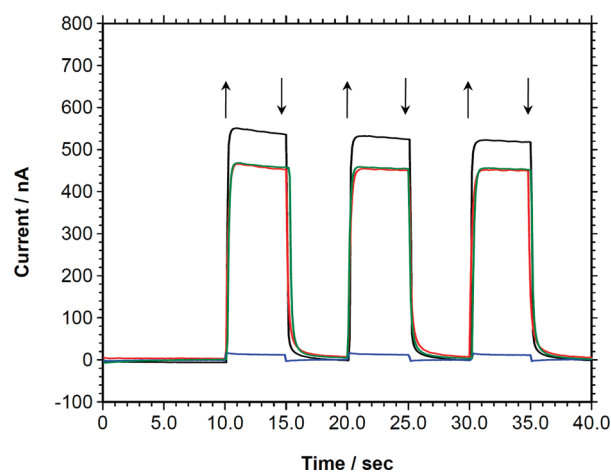
Figure 3. Example photoelectrochemical experiments of PQS silane films on ITO irradiated with ~2.3×10^{-5} einstein$\cdot$s^{-1} light intensity (435 nm $\leq \lambda \leq$ 475 nm). Light on = ↑. Light off = ↓. The blue trace represents i_B from a 3-day-old PQS silane film on ITO of 3.2×10^{-9} mol$\cdot$cm^{-2} coverage with no added NaBPh$_4$ in 100 mM NaCl at pH 7 with 1 mM MOPs. The black trace is the i_P photocurrent obtained for the same electrode in the presence of 1 mM NaBPh$_4$, corresponding to the $L = F = P = +1$ and $A = C = -1$ conditions listed in Table 1. The red trace indicates the i_P value observed in the presence of 1 mM NaBPh$_4$ for the same electrode aged 7 days and corresponds to $L = F = P = A = +1$ and $C = -1$ in Table 1. The green trace is the repeated i_P result for the 7-day-old electrode after nine intervening experiments. All photocurrents were recorded at -0.05 V versus Ag/AgCl.

Second, irreversible, unimolecular decay of the $BPh_4^\bullet$ radical to form BPh_3 and $Ph^\bullet$ radical can also occur, as shown in eq 6a

$$[PQ^+(X^-)(BPh_4^\bullet)] \rightarrow [PQ^+(X^-)(BPh_3)(Ph^\bullet)] \quad (6a)$$

$$[PQ^+(X^-)(BPh_3)(Ph^\bullet)] \rightarrow PQ^+X^- + BPh_3 + Ph^\bullet \quad (6b)$$
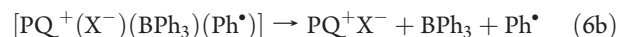
It has been suggested that reactions such as eq 6a proceed because decomposition of radicals such as $BPh_4^\bullet$ can occur at rates competitive with the rate of reverse electron transfer in eq 5, as shown by an observed buildup of the blue radical PQ^+ cation.[60,93] In addition, because reduction of the BPh_3 and $Ph^\bullet$ radical products by viologen cation radicals, such as MV^+, has not been observed,[60] diffusion of the neutral BPh_3 and the $Ph^\bullet$ radical products away from the reaction site can occur, as shown for the PQS film in the gray oval labeled 3 in Figure 1 and in eq 6b. As a result, accumulation of viologen monocation radical typically occurs during photolysis, at least in solution. Within the PQS film, this irreversible production of viologen monocation radical in the form of PQ^+ leads directly to photocurrent by electron transfer to the ITO electrode and regeneration of PQ^{2+} species, as shown in the gray oval labeled 4 in Figure 1 and in eq 7

$$ITO|PQ^+(X^-) + (X^- \text{ or } BPh_4^-) \rightarrow ITO^-|PQ^{2+}(X^-)(X^- \text{ or } BPh_4^-) \quad (7)$$
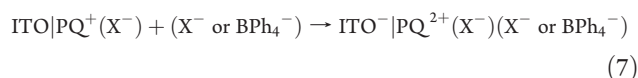
The ultimate fate of the highly reactive $Ph^\bullet$ radical is shown as dimerization, by analogy to its solution behavior,[60] to form biphenyl, as shown in the gray oval labeled 5 in Figure 1 and in eq 8

$$2Ph^\bullet \rightarrow Ph-Ph \quad (8)$$

Table 1. Summary of the Factorial Design Results

row^a	no.^{b}	L^c	F^d	C^e	P^f	A^g	i_N (nA)^h	i_P (nA)^h	i_B (nA)^h	ID^i	effect E^j	S^k
1	16	−1	−1	−1	−1	−1	58.80	63.33	4.53	average	172.8667	−
2	9	+1	−1	−1	−1	−1	213.43	225.33	11.90	L	195.3833	yes
3	6	−1	+1	−1	−1	−1	74.47	79.00	4.53	F	12.97917	no
4	2	+1	+1	−1	−1	−1	256.43	268.33	11.90	LF	5.520833	no
5	11	−1	−1	+1	−1	−1	40.13	44.66	4.53	C	−36.2333	yes
6	5	+1	−1	+1	−1	−1	140.00	149.00	9.00	LC	−9.95	no
7	10	−1	+1	+1	−1	−1	50.80	55.33	4.53	FC	11.72917	no
8	15	+1	+1	+1	−1	−1	177.33	186.33	9.00	LFC	4.354167	no
9	12	−1	−1	−1	+1	−1	151.97	155.33	3.36	P	123.0167	yes
10	13	+1	−1	−1	+1	−1	574.00	587.00	13.00	LP	70.8	yes
11	8	−1	+1	−1	+1	−1	203.97	207.33	3.36	FP	−10.7292	no
12	1	+1	+1	−1	+1	−1	524.67	537.67	13.00	LFP	−7.1875	no
13	7	−1	−1	+1	+1	−1	103.33	106.33	3.00	CP	−8.16667	no
14	14	+1	−1	+1	+1	−1	450.70	460.00	9.30	LCP	−4.71667	no
15	3	−1	+1	+1	+1	−1	117.00	120.00	3.00	FCP	11.6875	no
16	4	+1	+1	+1	+1	−1	452.37	461.67	9.30	LFCP	4.145833	no
17	26	−1	−1	−1	−1	+1	51.00	73.67	22.67	A	−102.942	yes
18	31	+1	−1	−1	−1	+1	131.00	235.33	104.33	LA	−53.175	yes
19	25	−1	+1	−1	−1	+1	57.67	80.33	22.66	FA	−2.60417	no
20	30	+1	+1	−1	−1	+1	160.33	264.66	104.33	LFA	12.9375	no
21	23	−1	−1	+1	−1	+1	24.33	46.00	21.67	CA	29.525	yes
22	28	+1	−1	+1	−1	+1	137.33	193.33	56.00	LCA	11.325	no
23	32	−1	+1	+1	−1	+1	35.33	57.00	21.67	FCA	11.47917	no
24	18	+1	+1	+1	−1	+1	173.33	229.33	56.00	LFCA	−6.72917	no
25	21	−1	−1	−1	+1	+1	91.33	148.66	57.33	PA	−72.8083	yes
26	20	+1	−1	−1	+1	+1	251.33	465.66	214.33	LPA	−37.0083	yes
27	27	−1	+1	−1	+1	+1	17.33	74.66	57.33	FPA	0.354167	no
28	17	+1	+1	−1	+1	+1	238.00	452.33	214.33	LFPA	13.72917	no
29	19	−1	−1	+1	+1	+1	50.67	115.00	64.33	CPA	8.875	no
30	22	+1	−1	+1	+1	+1	192.67	376.67	184.00	LCPA	−10.9917	no
31	24	−1	+1	+1	+1	+1	74.67	139.00	64.33	FCPA	8.770833	no
32	29	+1	+1	+1	+1	+1	256.00	440.00	184.00	LFCPA	−7.10417	no

^{a} Experiment number designation. ^{b} Order in which experiment was performed. ^{c} Coded light intensity levels by actinometry for 435 nm ≤ λ ≤ 475 nm: $L = −1 ≡ (6 ± 1) × 10^{−6}$ einstein·s$^{−1}$; $L = +1 ≡ (2.3 ± 0.5) × 10^{−5}$ einstein·s$^{−1}$. ^{d} Coded tetraphenylborate donor fuel levels in solution: $F = −1 ≡$ 0.1 mM NaBPh$_4$; $F = +1 ≡$ 1.0 mM NaBPh$_4$. ^{e} Coded anion (hydrophobicity and steric) designation levels: $C = −1 ≡$ chloride; $C = +1 ≡$ perchlorate. Anions are present as Na$^+$ salts at 100 mM concentration with 1 mM MOPS pH 7 buffer in aqueous solution. Hydrophobicity and steric designations are discussed in the text. ^{f} Coded PQ^{2+} acceptor coverage levels on PQS electrodes by coulometry: $P = −1 ≡ 9.54 × 10^{−10}$ mol·cm$^{−2}$; $P = +1 ≡ 3.18 × 10^{−9}$ mol·cm$^{−2}$. ^{g} Coded PQS electrode age levels measured from electrode preparation date: $A = −1 ≡$ 3 days; $A = +1 ≡$ 7 days. ^{h} Average current rounded to two decimal places (see Tables S-2 and S-3, Supporting Information). ^{i} Variables or combinations of variables associated with the experimental conditions described by the coded L, F, C, P, and A variable levels in the row. ^{j} Effect of the variable or combination of variables designated in the previous column on i_N as determined by Yates' algorithm analysis (see Table S-5, Supporting Information). ^{k} Significance at the 0.999 confidence level as determined by ANOVA (see Table S-6, Supporting Information). Designations: no ≡ not statistically significant; yes ≡ significant.

However, we cannot at this time preclude the possibility of other reactions of the Ph$^•$ radical within the PQS film, such as formation of benzene by hydrogen abstraction from available film silanol or methylene sites. Further work is in progress to identify and characterize such alternative reactions, if any, in connection with more detailed studies of PQS film stability that will be reported at a later date.

To characterize the performance of the cell described by Figure 1, the dependence of the photocurrent was examined as a function of five different variables using a two-level factorial design. In such a design, each variable is assigned a high and low value, coded as +1 and −1, respectively, and experiments are completed in random order under conditions reflecting each possible combination of variables. The set of 32 (i.e., 2^5) measured photocurrent responses obtained are statistically analyzed to provide values for the effect of each variable and combination of variables on the cell photocurrent. Statistically significant effects are then identified based on an analysis of the sample variance to provide a model for prediction of the cell photocurrent over the range of variables studied.

Table 1 summarizes the factorial design and results of its analysis. The entries in columns 3−7 in Table 1 summarize the design matrix, with each row representing an individual experiment identified by number in column 1 and an entry in column 2 indicating the (random) order in which the experiment was performed. Variables were chosen by analogy with the solution-

based $MV^{2+}(BPh_4^-)_2$ photoelectrochemical cell described previously[60] and observations of our system made during preliminary experiments. For example, the choices of light intensity (L), tetraphenylborate donor "fuel" concentration (F), and PQ^{2+} acceptor surface coverage (P) paralleled analogous variables known to influence photocurrents in the solution-based $MV^{2+}(BPh_4^-)_2$ photoelectrochemical cell, albeit with important differences. In particular, although the PQS film bearing covalently immobilized PQ^{2+} species used in our system exhibited reversible $PQ^{2+} \leftrightarrow PQ^+ + e^-$ electrochemistry in aqueous solutions, partially irreversible behavior was noted for the PQS electrode in acetonitrile solutions analogous to those of the solution-based $MV^{2+}(BPh_4^-)_2$ photoelectrochemical cell. This behavior limited our work to aqueous solutions, precluding measurement of any solvent dependence of the photocurrents or direct comparison of the performance of the two systems.

A key issue in the use of the PQS-covered ITO electrodes was the precise and reproducible control of the PQS surface coverage (P) corresponding to the +1 and −1 coded levels of the design. PQS coverage was determined during film deposition by the uniformity and conductivity of the ITO. Unfortunately, the range of conductivities associated with our ITO samples (see the Experimental Section) was sufficiently variable that it precluded fabrication of separate PQS-coated ITO electrodes for each of the 32 required design experiments. Therefore, single electrodes were separately prepared having P values of 9.54×10^{-10} and 3.18×10^{-9} (mol of PQ^{2+})$\cdot$cm^{-2} corresponding to the −1 and +1 coded design parameters, respectively, for reuse during the experiments. To limit contamination of the electrodes with the BPh_3 and Ph−Ph reaction products, which exhibit little or no solubility in water, an electrode rinsing protocol (see the Experimental Section) was developed and tested to prepare each electrode for reuse in subsequent experiments. Tests were made in which an electrode was used under a fixed initial set of experimental conditions, then rinsed and used in multiple intervening experiments under different experimental conditions, and finally rinsed and reused again under the same initial experimental conditions. Reproducible photocurrents were obtained for electrodes tested in this manner, as shown in the example of Figure 3, verifying the efficacy of the rinsing protocol.

Accumulation of reaction products at the electrodes was further minimized by the rather low levels of photocurrents drawn during the experiments (see Table 1), which were controlled in part by the nature of our equipment and the physicochemical properties of the reagents. For example, the light intensity (L) initiating photocurrent responses in our experiments was limited by the natural output of our lamp and the neutral density filters used to control intensity. In addition, because direct oxidation of BPh_4^- by the PQ^{2+} ($\pi-\pi^*$) excited state at ~280 nm readily occurs,[60] use of a 435-nm long-pass cutoff filter was necessary to isolate the tail of the weaker band at ~378 nm corresponding to the EDA complex (see Figure 2D) during exposure. Consequently, intensity values were restricted to $(6 \pm 1) \times 10^{-6}$ and $(2.3 \pm 0.5) \times 10^{-5}$ einstein$\cdot$s^{-1}, corresponding to the −1 and +1 coded L parameters, respectively, in the 435 nm $\leq \lambda \leq$ 475 nm wavelength range associated with the absorbance of the EDA complex in our experiments. Cell photocurrent outputs were additionally limited by the low solubility of the donor $NaBPh_4$ fuel (F) in aqueous solution (~1 mM) compared to the acetonitrile solutions used with the solution-based $MV^{2+}(BPh_4^-)_2$ photoelectrochemical cell.[60] Specifically, available $NaBPh_4$ levels were restricted to a narrow

range spanning values of 0.1 and 1.0 mM, corresponding to coded F levels of −1 and +1, respectively, in our system.

Two additional variables not usually considered in the operation of photoelectrochemical cells, the PQS electrode age (A) and the nature of the electrolyte counterion (C), were also chosen for study in the factorial design of Table 1. The choice of electrode age was made based on the siloxane cross-linking reaction previously identified as the mechanism for PQS film deposition.[68] In particular, the kinetic control associated with the rapid cross-linking of free silanol species formed by electrochemically promoted hydrolysis of the PQS trimethoxysilane (see Scheme 1) provides a porous PQS siloxane network having numerous unreacted silanol species, at least initially. Hydrolysis of a fraction of silanols to form anionic Si−O$^-$ sites capable of affecting ion diffusion, and consequently also photocurrent, within the PQS film might therefore occur under our experimental conditions at pH 7, given the known silanol p$K_a \approx$ 6.5−7.0.[94,95] As the electrode ages and these unreacted silanols eventually cross-link, changing the internal charge and structure of the PQS film, associated changes in photocurrents are also expected. To allow sufficient time for the PQS electrode structure to equilibrate following deposition, we selected electrodes aged for 3 and 7 days, coded in Table 1 as −1 and +1, respectively, for study to examine these effects.

Our selection of the nature of the electrolyte counterion (C) as the final variable for study was prompted by the results of preliminary experiments shown in Figure 2C (inset). In these experiments, differences in the variation of the PQS electrode current with added solution $NaBPh_4$ levels were observed for solutions containing NaCl or $NaClO_4$ as the supporting electrolyte. Equilibrium constants, estimated using eq 3 for the BPh_4^- ion-exchange process, indicated that the Cl$^-$ ion ($K_{chloride}$ = 38000 M^{-1}) was somewhat more readily displaced by BPh_4^- than the ClO_4^- ion ($K_{perchlorate}$ = 31000 M^{-1}) in the PQS electrode environment. This behavior suggested to us that differences in hydrophobicity and/or size of the electrolyte anion could influence the binding of BPh_4^- to the PQ^{2+} sites to form the requisite EDA complex within the PQS films and, therefore, also the cell photocurrent. Hydrophobicity has been previously correlated to ion Jones−Dole viscosity B coefficients, which provide a numerical measure of ion−water affinity related to the nature of the ion's water solvation shell,[96] whereas steric effects can be approximated from ionic radii, r. Therefore, we adopted B coefficients[97] and ionic radii[98] as measures of anion hydrophobicity and size, respectively, for discussion of the C parameter in our design. These formally correspond to values for chloride of $B = -0.005$ and $r = 181$ pm and for perchlorate of $B = -0.058$ and $r = 244$ pm as the −1 and +1 levels for C, respectively, in the design in Table 1.

It is interesting to note that photocurrents generated in the acetonitrile-solution-based $MV^{2+}(BPh_4^-)_2$ photoelectrochemical cell[60] were observed to depend on the nature of the electrolyte cation, suggesting that ion pairing between the electrolyte cation and BPh_4^- also influences EDA complex formation. Unfortunately, precipitation of BPh_4^- in the presence of cations such as K$^+$ or Cs$^+$ in our aqueous solutions precluded study of the any similar cation effects on the cell photocurrent in our system. Therefore, the electrolyte cation was fixed as Na$^+$ for all experiments involving our photoelectrochemical cell.

The remaining entries in Table 1 summarize the results and analyses of the experiments. Specifically, column 8 lists the average net photocurrent, i_N, obtained for each experiment and
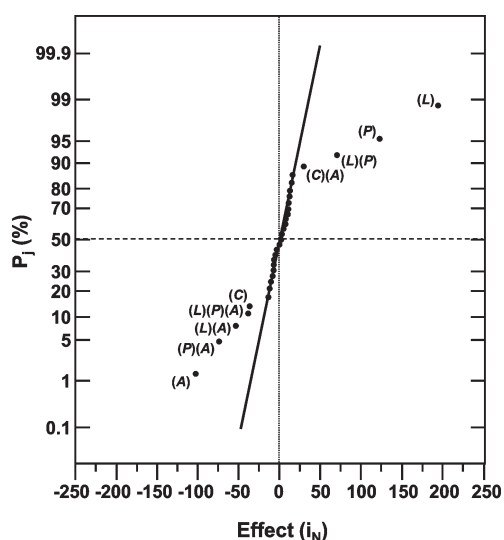
Figure 4. Normal probability plot. Variables and variable interactions associated with statistically significant photocurrent effects are indicated by data points deviating from the straight line formed by the variable(s) exhibiting nonsignificant effects. Data were taken from Table S-7 of the Supporting Information. Variables associated with significant effects are identified by one or more letters according to the nomenclature of Table 1.

Figure 5. Photoelectrochemical cell response maps. Geometric representation of the influence of the L, P, and A variables on the average cell response as described in the text. (A) Chloride electrolyte $(C = -1)$, (B) perchlorate electrolyte $(C = +1)$.

analyzed in the design. Because the PQS-coated ITO electrode registers a weak photocurrent response in the absence of added NaBPh$_4$, an average blank photocurrent, i_B (see column 10), was measured for each set of design conditions and subtracted from the corresponding average photocurrent obtained for the same solution containing NaBPh$_4$, i_P (see column 9), to obtain the i_N value. The average i_P and average i_B values were calculated from individual measurements summarized in the Supporting Information (see Tables S-2—S-4). The effects due to each variable or combination of variables, as identified in column 11, were calculated using Yates' algorithm[86] as illustrated in Table S-5 (Supporting Information) and reported in column 12, together with the grand average photocurrent for the set of experiments (i.e., row 1, column 12). Finally, column 13 identifies those effects that are statistically significant at the 0.999 confidence level, as calculated from the analysis of variance (ANOVA) using the information shown in Tables S-3, S-4, and S-6 (Supporting Information). Significant effects are identified as those having calculated F-distribution values (i.e., F_0, Table S-6, Supporting Information) greater than the corresponding expected value taken from an F-distribution table (i.e., F_c, Table S-6, Supporting Information),[87] as discussed in the Supporting Information. In Table 1, an entry of "no" in column 13 identifies an effect that is not significant and is therefore attributed to random experimental error. An entry of "yes" corresponds to an effect that is significant, indicating that the associated variable or combination of variables does influence i_N.

An examination of the results of the factorial analysis in Table 1 reveals three important points concerning our system. First, none of the effects found significant were associated with variable F corresponding to the donor concentration in solution, $[BPh_4^-]$. This is clearly illustrated in the half-normal plot shown in Figure 4, prepared as described in the Supporting Information (see Table S-7), in which significant effects deviate from the straight line defined by the nonsignificant effects, consisting in
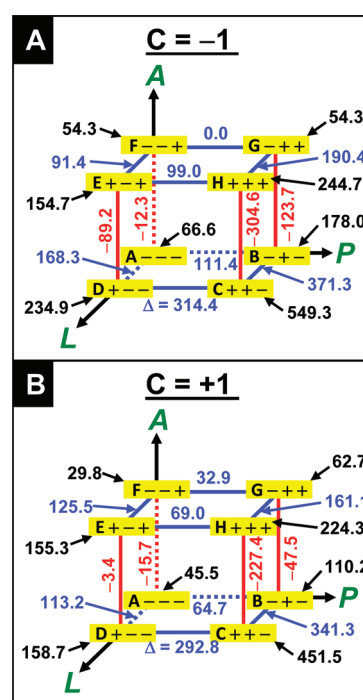
part of effects due to F and its various interactions with the other variables. This behavior contrasts with that of the acetonitrile-solution-based $MV^{2+}(BPh_4^-)_2$ photoelectrochemical cell,[60] for which the BPh_4^- concentration influences the observed photocurrent. However, the behavior of our aqueous cell is not surprising given (1) the limited aqueous solubility of NaBPh$_4$ that restricts its range of study here to just 0.1—1.0 mM and (2) the BPh_4^- anion's strong interaction with PQ^{2+} sites within the PQS film. In particular, Figure 2C (inset) indicates that BPh_4^- binding within the PQS film is nearly complete even at a 0.1 mM NaBPh$_4$ in both chloride and perchlorate electrolyte solutions and essentially equivalent to that observed at 1.0 mM NaBPh$_4$. Consequently, minimal i_N variations consistent with a nonsignificant F effect are expected, given the nearly equivalent amounts of the tetraphenylborate—viologen EDA complex formed for the 0.1 and 1.0 mM NaBPh$_4$, with all other variables held constant.

Second, the most significant effects in Table 1 and Figure 4 are those attributed to light intensity (L), PQ^{2+} coverage in the PQS electrode (P), and PQS electrode age (A), which predominantly determine the magnitude of i_N obtained for a given experiment. Positive effects associated with L and P indicate that increases in the magnitudes of these variables increase i_N, whereas the negative effect associated with A leads to decreased i_N as the electrode ages. Although no age effects have been reported for the Pt electrode used in the acetonitrile-solution-based $MV^{2+}(BPh_4^-)_2$ photoelectrochemical cell,[60] that cell exhibits general increases in photocurrent with increased light intensity and soluble MV^{2+} concentration consistent with analogous behaviors for our cell described here.

Third, a key finding from the analysis of the factorial design is that the effects of the major variables L, P, and A on i_N are also complex. Specifically, the presence of significant effects associated

with the cross terms, LP, CA, PA, LA, and LPA indicates that significant interactions among the L, P, A, and C variables occur in our cells. Consequently, variations in the observed i_N value with changes in the magnitude of any one of these variables will depend on the values of the remaining variables. These variations are readily illustrated using standard geometric representations, which provide a convenient means to globally visualize complex systems such as ours and map the critical i_N response trends as functions of the significant variables and their interactions.[86]

Figure 5 provides one such representation for visualization of the major effects due to the L, P, and A variables on the i_N value at each fixed level of C. In each case, these variables form a set of mutually orthogonal axes defining a cube whose vertices are each identified by a capital letter and sequence of three consecutive + and/or − symbols representing, in order, the levels of the L, P, and A variables. For example, in each cube vertex A having a $(- - -)$ designation represents the condition in which variable levels are $L = -1$, $P = -1$, and $A = -1$, whereas vertex F having a $(- - +)$ designation corresponds to variable levels of $L = -1$, $P = -1$, and $A = +1$. The values in black text associated with each vertex represent the average i_N value associated with the specified levels of the L, P, A, and C variables, with the average taken over the ± 1 levels of the nonsignificant F variable in Table 1. For example, the 54.3 value at the vertex F [i.e., $(- - +)$] in Figure 5A represents an approximation for i_N at the $L = P = -1$, $A = +1$, and $C = -1$ conditions and corresponds to the arithmetic average of the i_N from rows 17 (i.e., $F = -1$) and 19 (i.e., $F = +1$) of Table 1, whereas the 549.3 value at vertex C [i.e., $(+ + -)$] is the arithmetic average of rows 10 (i.e., $F = -1$) and 12 (i.e., $F = +1$) describing the $L = P = +1$, $A = -1$ and $C = -1$ conditions. Values for other vertices were calculated similarly. Note that the viability of the method requires that averages be taken only over variables associated with nonsignificant effects, a requirement met here by limiting averages to F terms and isolating the significant C term through separate representations for each of its −1 and +1 levels.

Figure 5A,B can be used to approximate changes and identify trends in the i_N response as L, P, and A are changed at each level of C in our system. Approximate variations in i_N as the levels of L, P, or A are changed at each level of C, averaged over the nonsignificant F values, are shown by the Δ values associated with the edges of each cube. These values represent average changes expected for i_N on proceeding from the −1 to the +1 level of the variable changing along the edge at constant levels of the remaining two variables, with increases in i_N shown as blue text and lines and decreases in i_N shown as red text and lines. For example, the $\Delta = 314.4$ nA value corresponds to cube edge DC in Figure 5A. The P value changes from −1 to +1 along this edge, whereas L and A remain constant at their +1 and −1 levels, respectively. Therefore, $\Delta = 314.4$ nA is calculated by subtraction of the i_N value at vertex D with $P = -1$ from the i_N value at vertex C with $P = +1$ and represents the approximate increase in i_N averaged over the $F = \pm 1$ levels as P is increased from its −1 to +1 levels at constant $L = +1$ and $A = C = -1$ levels. In similar fashion, $\Delta = -89.2$ nA (i.e., $154.7 - 249.3$ nA) for edge DE indicates the approximate decrease in i_N expected as A increases from its −1 to +1 level at constant $L = +1$ and $P = C = -1$ levels.

Comparison of the i_N values associated with the various vertices, lines, and faces in each cube provides an estimate of the influence of the L, P, and A variables on the cell performance averaged over the $NaBPh_4$ concentration levels (i.e., $F = \pm 1$) in our experiments. For example, the ABCD cube face in Figure 5A contains information defining the average i_N value expected as L

and P are varied at constant $A = C = -1$, representing a cell having a 3-day-old electrode using chloride electrolyte. Averaged photocurrent values corresponding to each of the A (i.e., 66.6 nA), B (i.e., 178.0 nA), C (i.e., 549.3 nA), and D (i.e., 234.9 nA) vertices are generally substantial, with increases in L or P or both L and P simultaneously accompanied by strong increases in photocurrent, as indicated by the magnitudes of the Δ values and the blue edges of the cube defining the ABCD face. For example, $\Delta = +168.3$ nA along edge AD represents the average increase in i_N due to an increase of light intensity L from its −1 to +1 level at constant $P = A = -1$ levels corresponding to a 3-day-old electrode having low PQS coverage. For the corresponding high-PQS-coverage electrode, $P = +1$ of equivalent 3-day age $A = -1$, the increase of i_N as L changes from the −1 to +1 levels is $\Delta = +371.3$ nA as shown by edge BC. The Δ values along edges AB (111.4 nA) and DC (314.4 nA) provide comparisons of the effect of changing PQS electrode coverage from low $P = -1$ to high $P = +1$ values at low $L = -1$ and high $L = +1$ light levels, respectively, for the same $A = -1$ 3-day-old electrode. These large average i_N values and positive Δ values identify and provide a useful map of the LP interaction for the $A = C = -1$ cell conditions.

Cube face FGHE in Figure 5A provides analogous information concerning the nature of the LP interaction for the 7-day-old PQS electrode in chloride media identified by the $A = +1$ and $C = -1$ levels. Within the FGHE face, representing the 7-day-old electrode with $A = +1$, the variations in estimated i_N value with changes in the L and P levels are smaller than the analogous variations for the 3-day-old electrode with $A = -1$ in face ABCD. However, similar overall trends are observed, as expected for an LP interaction. For example, i_N is increased by $\Delta = +91.4$ nA (edge FE) and 190.4 nA (edge GH) as L is increased from −1 to +1 at constant $P = -1$ and $P = +1$, respectively. These values are each significantly less than the corresponding Δ values of +168.3 nA (edge AD) and 371.3 nA (edge BC) for the 3-day-old electrode having $A = -1$ represented by face ABCD.

The differences found as P is increased from its −1 to +1 levels at constant $L = -1$ and $L = +1$ levels is even more striking. At high light levels where $L = +1$, increased PQS electrode coverage yields $\Delta = +99.0$ nA (edge EH), which is again significantly less than the $\Delta = 314.4$ nA (edge DC) calculated for an analogous change at the $A = -1$ level. In contrast, at low light levels where $L = -1$, there is essentially no estimated change in average photocurrent (i.e., $\Delta = 0.0$ nA, edge FG) compared to a $\Delta = 111.4$ (edge AB) at the $A = -1$ level. These comparisons indicate that, although still present, the LP interaction is generally diminished as the electrode ages, consistent with the presence of the negative LPA effect previously noted in Table 1 and Figure 4. In similar fashion, separate comparisons of faces ADEF to BCHG and ABGF to DCHE in each cube map the LA and PA interactions, respectively, for our cell.

Given the smaller magnitudes of their effects, the influences of the C variable and CA interaction are less obvious, although still discernible, in Figure 5A,B. In particular, comparison of the average i_N value associated with each vertex of Figure 5A with the same vertex of Figure 5B corresponds to a change of C from its −1 to +1 level at the fixed L, P, A, and $F = \pm 1$ average levels specified by the vertices. For example, $i_N = 234.9$ and 158.7 nA at vertex D and $i_N = 244.7$ and 224.3 nA at vertex H in parts A and B, respectively, of Figure 5. With the exception of vertex G, for which $i_N = 62.7$ nA in Figure 5B exceeds $i_N = 54.3$ nA in Figure 5A, the i_N value for each vertex in Figure 5A corresponding to
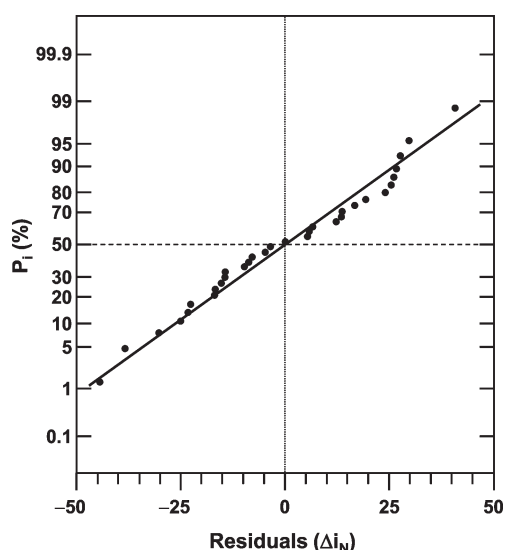
13456

dx.doi.org/10.1021/jp2023988 |J. Phys. Chem. C 2011, 115, 13446–13461

Figure 6. Residuals probability plot for the model of eq 9. Consult Tables S-8—S-10 of the Supporting Information for details on the calculation of the residuals and the article text for additional information.

$C = -1$ exceeds the i_N value for the same vertex in Figure 5B corresponding to $C = +1$. Such behavior is consistent with and expected given the statistically significant negative C effect noted in Table 1 and Figure 4.

In similar fashion, evidence for the positive CA interaction is summarized in the Δ values associated with the -1-to-$+1$ transition for A, which is represented by edges AF, BG, CH, and DE in each cube. Specifically, the Δ values for each edge in Figure 5B (i.e., $C = +1$) are less negative than those for the same edge in Figure 5A (i.e., $C = -1$). For example, $\Delta = -89.2$ and -3.4 nA for edge DE and -123.7 and -47.5 nA for edge BG in parts A and B, respectively, of Figure 5. Therefore, for each edge representing a -1-to-$+1$ A transition, the change in average i_N value represented by its Δ value becomes less negative (i.e., more positive) as C is changed from its -1 to $+1$ level, consistent with the small positive CA effect noted in Table 1 and Figure 4.

Based on these observations, it is clear that i_N values for cells using chloride electrolyte (i.e., $C = -1$) are far more sensitive to electrode age than those using perchlorate (i.e., $C = +1$). Specifically, although the i_N values for chloride cells are larger than those for the perchlorate cells when the electrode is 3 days old, as shown by pairwise comparison of the same vertices in parts A and B of Figure 5, their decreases as measured by Δ values for the corresponding edges are also greater as the electrode age increases to 7 days. In fact, nearly equivalent average photocurrents are noted for electrodes aged 7 days under otherwise identical L and P conditions in Figure 5A,B. For example, we observed average i_N values of 54.3 and 29.8 nA at vertex F (i.e., $L = P = -1$, $A = +1$) and 244.7 and 224.3 nA at vertex H (i.e., $L = P = A = +1$) in parts A and B, respectively, of Figure 5. This behavior suggests that differences between the chloride and perchlorate electrolytes, whatever their nature, generally become less significant as the electrode ages and reaches a thermodynamic equilibrium state in which internal siloxane cross-linking reactions are substantially completed and further underscores the complex nature of the electrolyte interaction.

Although geometric representations are convenient to map and observe general cell response trends, the factorial analysis

also provides the means for quantitative modeling of the behavior of i_N as functions of the variables and variable interactions associated with the significant effects in Table 1 and Figure 4. The significant effects in Table 1, together with the grand average, define such a model for the prediction of the net photocurrent, i_N, for any combination of experimental conditions within the ranges of the significant variables studied. From Table 1, the model takes the form of eq 9 in which photocurrent values are computed as deviations from the grand average weighted by the product of the sign and magnitude of each significant effect and the coded values of its associated variables.

$$i_N \text{ (nA)} = 172.8667 + \frac{1}{2}(195.3833L + 123.0167P + 70.8LP$$
$$+ 29.525CA - 102.942A - 72.8083PA - 53.175LA$$
$$- 37.0083LPA - 36.2333C) \tag{9}$$

Equation 9 can be used to calculate an estimated i_N value for each of the experimental conditions in Table 1, as described in detail in the Supporting Information (see Tables S-8 and S-9). The difference between the i_N value estimated by eq 9 and the corresponding average i_N value measured for each experiment in Table 1 yields a residual, Δi_N [calculated as (estimated i_N) − (average i_N)], that provides a measure of the ability of the model to predict the i_N value. The normal probability plot of Δi_N shown in Figure 6, calculated as described in the Supporting Information (see Table S-10), yields a straight line about $\Delta i_N = 0$, indicating that eq 9 provides a reasonable model for prediction of the i_N values, at least for conditions where variable levels are at or near their ± 1 levels.

A further test of the model involves comparisons of measured photocurrents for conditions corresponding to variable levels intermediate between the -1 and $+1$ range to those calculated using eq 9, as summarized in Table 2. Because our model is based on a two-level factorial design, its ability to exactly predict such i_N responses requires that the measured photocurrent response vary linearly with the coded value of each variable within its -1 to $+1$ range per eq 1. When the i_N response is nonlinear, reasonable approximations can still be made provided that the functional form of the variation is monotonic and its deviation from linearity is small. For example, from Table 2 (row 1), we measured $i_N = 239.8$ nA in a cell containing 1 mM NaBPh$_4$ in the perchlorate electrolyte solution using a 3-day-old electrode having high PQS film coverage at 50% of maximum light intensity. These conditions correspond to variable levels of $L = -0.401$, $F = C = P = +1$, and $A = -1$, where eq 1 was used to calculate the = -0.401 coded L level corresponding to 50% light intensity. Using these same coded variable levels, eq 9 estimates $i_N = 217.2$ nA, in good agreement with the measured i_N value, with a deviation (-22.6 nA or -9.4%) well within the range of uncertainties (see Figure 6) associated with our model. In similar fashion, irradiation of 0.5 mM NaBPh$_4$ in the perchlorate electrolyte solution using a 3-day-old electrode having high PQS film coverage at full light intensity, corresponding to $L = +1$, $F = -0.1111$, $C = +1$, $P = +1$, and $A = -1$ in row 2 of Table 2, yields a measured value of $i_N = 515.7$ nA. The $i_N = 467.6$ nA value calculated from eq 9 represents a deviation of -48.1 nA (-9.3%), again in reasonable agreement with the measured i_N value. In addition, photocurrents obtained for intermediate PQS film coverage levels (i.e., $P = 0.0117$) for cells utilizing either chloride or perchlorate electrolyte are also well predicted by the model, at least for the 3-day-old electrode, as shown for the examples in rows 3 and 6 in Table 2.

13457

dx.doi.org/10.1021/jp2023988 |*J. Phys. Chem. C* 2011, 115, 13446–13461

Table 2. Photocurrent Measurements and Calculations at Intermediate Levels of Variables

row[b]	variable levels[a]					i_N (nA)		Δi_N (nA) (%)[e]
	L	F	C	P	A	observed[c]	model[d]	
1	−0.405[f]	1	1[g]	1	−1	239.8	217.2	−22.6 (−9.4)
2	1	−0.1111[h]	1	1	−1	515.7	467.6	−48.1 (−9.3)
3	1	1	−1[i]	0.0117[j]	−1	422.0	383.3	−38.7 (−9.2)
4	1	1	−1	0.0117[j]	0.5000[k]	307.3	243.0	−64.3 (−20.9)
5	1	1	−1	0.0117[j]	1	261.7	196.0	−65.7 (−25.1)
6	1	1	1	0.0117[j]	−1	351.0	317.5	−33.5 (−9.7)
7	1	1	1	0.0117[j]	0.5000[k]	233.3	222.0	−13.3 (−4.9)
8	1	1	1	0.0117[j]	1	132.0	189.0	57.0 (43.2)
9	1	1	0.0566[l]	0.0117[j]	−1	421.0	348.5	−72.5 (−17.2)
			−0.7087[m]				373.7	−47.3 (−11.2)
10	1	1	0.0566[l]	0.0117[j]	0.5000[k]	272.7	234.7	−38.0 (−14.0)
			−0.7087[m]				239.9	−32.9 (−12.1)
11	1	1	0.0566[l]	0.0117[j]	1	219.3	192.8	−26.5 (−12.1)
			−0.7087[m]				191.5	−27.8 (−12.7)
12	1	−1	0.4340[n]	0.0117[j]	−1	375.0	335.9	−39.1 (−10.4)
			0.3010[o]				340.5	−34.5 (−9.2)
13	1	−1	0.4340[n]	0.0117[j]	0.5000[k]	203.3	227.7	24.4 (12.0)
			0.3010[o]				229.1	25.8 (12.7)
14	1	−1	0.4340[n]	0.0117[j]	1	136.0	191.5	55.5 (40.8)
			0.3010[o]				192.0	56.0 (41.2)

[a] Coded variable levels for each experiment. Levels other than those designated −1 or +1 were calculated from the experimentally measured (or selected) low and high values of the variable defining its −1 and +1 coded levels, respectively, and its experimentally measured (or selected) value intermediate between its low and high values using eq 1. [b] Experiment number. [c] Measured photocurrent i_N (nA) for the experimental conditions defined by the levels of L, F, C, P, and A in columns 2−6. Consult Supporting Information Tables S-11 and S12 for data. [d] Photocurrent i_N (nA) calculated from the model of eq 9 using the coded variable levels in columns 2−6. [e] Deviation (nA) between the measured photocurrent and the photocurrent determined from the model of eq 9 calculated as $\Delta i_N = i_N$(model) − i_N(observed). Values in parentheses are percentage deviations relative to i_N(observed). [f] Coded level corresponding to an experimental light intensity of $1.1 \pm 0.1 \times 10^{-5}$ einstein·s^{-1} obtained using the 50% transmission neutral density filter. [g] Coded level corresponding to perchlorate electrolyte having B = −0.058 and r = 284 pm. [h] Coded level corresponding to an experimental value of [NaBPh$_4$] = 0.5 mM. [i] Coded level corresponding to chloride electrolyte having B = −0.005 and r = 181 pm. [j] Coded level corresponding to a PQS electrode with a viologen coverage of 2.08×10^{-9} mol·cm^{-2}. [k] Coded level corresponding to a 6-day-old PQS electrode. [l] Coded level corresponding to the B = −0.033 Jones−Dole viscosity parameter as a measure of hydrophobicity for the bromide anion. [m] Coded level corresponding r = 196 pm for the ionic radius as a measure of the steric hindrance of the bromide anion. [n] Coded level corresponding to B = −0.043 for the Jones−Dole viscosity parameter as a measure of hydrophobicity for the nitrate anion. [o] Coded level corresponding to r = 248 pm for the ionic radius as a measure of the steric hindrance of the nitrate anion.

As the cell electrode ages, however, the agreement between measured and predicted photocurrents diminishes somewhat (see rows 3−8, Table 2), although the model still correctly predicts the general trend of decreased i_N observed with increased age, A. Such behavior is not unexpected, given the number, complexity, and strengths of the interactions between A and the L, P, and C variables identified in Table 1 and Figure 4. In particular, as demonstrated in Figure 5, the dominant effects of L and P are diminished as A increases even as uncertainties inherent in the measurements of the decreased i_N value and our model (see Figure 6) become more pronounced, rendering i_N predictions less reliable. However, despite such behavior and its tendency to generally underestimate the i_N value somewhat, the model nevertheless provides reasonable i_N estimates for intermediate levels of these variables.

The same factors limiting the ability of the model to predict i_N for increasingly positive levels of A also affect our analysis of the C variable. In particular, i_N values predicted by our model are not very sensitive to changes in the level of C, which corresponds to the use of electrolytes other than chloride or perchlorate in the cell, because of the lower magnitudes and opposing signs of the effects associated with the C variable and CA interactions. In addition, for older electrodes represented by more positive A levels, the magnitudes of the measured i_N values approach the levels of uncertainty associated with model calculations (see Figures 5 and 6), resulting in a worsening signal-to-noise ratio that further complicates the analysis.

These limitations are illustrated in Table 2 for cells operated with bromide (rows 9−11) or nitrate (rows 12−14) electrolyte (see also Tables S-11 and S-12 for data and calculations). Appropriate levels of C were calculated separately from eq 1 for each electrolyte (Table 2, footnotes) using Jones−Dole viscosity B coefficients[97] and ionic radii (r)[98] as representations for hydrophobicity and steric effects, respectively, previously identified as anion parameters potentially affecting i_N (vide supra, Figures 1 and 2C, inset). From these levels, predicted i_N values were calculated in each case using eq 9. As expected, little difference between the i_N values calculated using the B coefficient and r is noted, consistent with our arguments concerning limited sensitivity of the model to variations in the level of C arising from weak, opposing effects due to the C variable and CA interaction.

We do note, however, that measured i_N values decrease with increased electrode age for both bromide and nitrate cells, consistent with our observations for the chloride and perchlorate electrolytes, and that discrepancies between measured and calculated i_N values are consistent with those observed in chloride and perchlorate cells having electrodes of the same age, A. Furthermore, comparisons of the bromide, chloride, and perchlorate results obtained under identical experimental conditions in Table 2 indicate that the measured i_N value for the bromide cell lies between those obtained for the chloride and perchlorate cells in each case. Such behavior is certainly expected if C is properly represented by and is a measure of the effect of either anion hydrophobicity or size on the i_N value for our cells. However, although the presence of significant C and CA effects identifies electrolyte as a real contributor to cell performance, our limited photocurrent results and model are presently insufficient to determine the nature of the B coefficient and/or r contribution in our cells, if any. Additional experiments involving a wider variety of electrolyte anions, together with larger-area electrodes having greater PQS film coverage irradiated at higher light intensities (see Figure 5A,B), will clearly be required to obtain i_N values with the improved signal-to-noise ratios necessary to discriminate anion effects due to the C variable. Therefore, although the limited results in Table 2 might suggest otherwise, we cannot at this time recommend the use of eq 9 for the description of photoelectrochemical cells using electrolytes other than chloride or perchlorate.

Our observations and analyses summarized in Tables 1 and 2 and Figures 4−6 suggest a straightforward aging model for the electrode PQS film of Figure 1. During deposition of PQS onto the ITO electrode, kinetic control of the organosilane hydrolysis reaction initially results in a loosely cross-linked siloxane film that defines the ultimate siloxane network. In this nascent film many, but not all, of the available hydrolyzed silanols have condensed to form Si−O−Si cross-linker species. The remaining unreacted silanols initially persist and, together with Si−O$^-$ anions formed by Si−OH deprotonation in our pH ∼7 solutions, interact with accessible PQ^{2+} sites and solution electrolyte components (see Figure 1). The presence of such dangling silanol-terminated groups therefore affects both i_N and i_B in the cell. For example, background photocurrents (i_B) are due to photoredox reactions of electrolyte components at the ITO surface because there are no chromophores capable of absorbing the visible light ($\lambda \geq$ 435 nm) used in our experiments within the PQS films in the absence of BPh_4^-. Therefore, the magnitude of i_B will be controlled by the rate of electrolyte diffusion to the ITO surface, which will be decreased by electrolyte interactions with any dangling silanol-terminated groups in the film, resulting in relatively low i_B values as observed for the 3-day-old electrodes in Table 1.

In contrast, given its hydrophobicity and propensity to ion pair with alkali metal cations such as Na$^+$,[99] the BPh_4^- anion should be less affected by hydrogen-bonding or electrostatic interactions with these free Si−OH and Si−O$^-$ species. The ability of the large BPh_4^- anion (see Scheme 1) to penetrate the film and form EDA complexes further suggests that (1) the dangling silanol-terminated species do not pose a serious steric hindrance to electrolyte anions and (2) their associated viologen sites remain readily accessible. Under such conditions, relatively large i_N values are expected, as observed in Table 1 for the 3-day-old electrodes.

As the electrode ages, condensation of free silanols to form additional Si−O−Si siloxane bonds will continue subject to physical constraints of the existing siloxane network. Specifically, reaction of nearby silanols within a given cluster of existing siloxane structures will be favored, rather than condensations bridging neighboring siloxane structures (see Figure 1, red dashed line box) that would reduce film porosity. This conclusion is supported by electrochemical measurements that indicate that the ability of redox-active solution species of various size and charge to penetrate the PQS film, and therefore also film porosity, is little changed as the electrode ages (see Supporting Information Figure S-1 and Table S-1). Therefore, as levels of free Si−OH and Si−O$^-$ species capable of interacting with solution ions are reduced without significant diminution of film porosity, enhanced electrolyte diffusion rates accompanied by increased i_B values should occur. In fact, Table 1 indicates that such increases in i_B do occur as our electrodes age, consistent with our model.

At the same time, stresses accompanying formation of these new siloxane bonds in an increasingly constrained film environment can be relieved, at least in part, by conformational changes within the propyl chain and viologen components. Given the increasingly constrained environment near the viologen posed by the formation of these additional siloxane bonds, however, net inhibition of tetraphenylborate−viologen EDA complex formation is likely. For example, increased steric effects that limit access of BPh_4^- to the viologen, local hydrophobicity changes that alter the ability of BPh_4^- to displace anions bound to the viologen, or changes in the conformation of the pyridinium rings of the viologen each could inhibit EDA complex formation. Although our results are not sufficient to determine which possibility, if any, occurs in our PQS films, all lead to reduced i_N values as the electrode age increases, consistent with our observations from Table 1.

■ CONCLUDING REMARKS

Although a photoelectrochemical cell utilizing an EDA complex prepared by the interaction of tetraphenylborate anion with a viologen electrode comprises a conceptually simple system for study, appearances are clearly deceiving. Results of two-level factorial design experiments confirm that photocurrent increases significantly with increasing light intensity (L) and/or viologen coverage (P), in agreement with the behavior of an analogous solution-based photoelectrochemical cell.[60] However, the analysis also identifies electrode age (A) as a major contributor to the observed photocurrent, with increased age leading to decreased photocurrent in opposition to the effects of L and P. The observed age effect is consistent with observations from experiment and suggests a model in which continued siloxane bond formation as the electrode ages increasingly isolates the viologen sites, making formation of the EDA complex more difficult and leading to decreased photocurrents.

At the same time, although no significant dependence of photocurrent on solution tetraphenylborate levels (F) was observed over the range of BPh_4^- concentrations investigated here, a weak antagonistic effect associated with the nature of the electrolyte anion (C) is noted. The system is further complicated by the presence of synergistic LP and CA and antagonistic LA, PA, and LPA variable interactions not identified in the analogous solution-based cell.[60] Nevertheless, the factorial analysis provides a model in the form of eq 9 that reliably predicts photocurrent

13459

dx.doi.org/10.1021/jp2023988 |J. Phys. Chem. C 2011, 115, 13446−13461

responses as functions of the levels of the major L, P, and, to a somewhat lesser extent, A variables over the ranges of these variables investigated here. Inherent uncertainties arising from experimental error associated with the model preclude a detailed analysis and understanding of the nature of the C effect at this time and are also responsible for its decreased accuracy in predicting photocurrents for older electrodes.

Maps illustrating the average effects of the L, P, and A variables clearly indicate that optimization of cell photocurrent response will require the use of larger-area electrodes of higher PQS coverage and more intense illumination. They further confirm the deleterious effects of electrode aging on photocurrent response and clearly identify aging as a key factor ultimately limiting cell performance. Given our observations and analyses, stringent control of the siloxane bond formation process associated with PQS film aging will be required to sufficiently stabilize the initial film structure associated with higher photocurrent outputs.

Our results suggest at least two possible approaches to achieve this goal. One involves a molecular templating process in which tetraphenylborate−viologen EDA complexes are formed in a freshly prepared PQS film prior to thermal annealing. The presence and steric hindrance of the EDA complex during the annealing process provides a means to potentially limit both the conformational mobility of the viologens and siloxane bond formation in their immediate vicinity, thereby preserving access to the viologen sites by BPh_4^- following completion of siloxane bond formation.

Alternatively, introduction of nonreactive trimethylsilyl "caps" through silanol reaction with reagents such as hexamethyldisilazane might additionally hinder the siloxane cross-linking process to preserve the initial film structure associated with generation of higher photocurrents. Capping in this manner might also stabilize the PQS film electrode for use in polar aprotic solvents, extending the range of applicability of the cell and photochemical reactions that can be driven by it. We are pursuing these and related research avenues to further understand and optimize the performance of our tetraphenylborate−viologen photoelectrochemical cells, as well as extend their applicability to more complex systems including photosensitizers capable of absorbing a greater fraction of the visible/IR spectrum to enhance output of these types of cells.

■ ASSOCIATED CONTENT

ⓢ Supporting Information. Figure and table providing probe structures, dimensions, and photocurrent measurements related to determination of the film pore size and description of the calculations associated with analysis of the factorial design experiments with tables listing the results of intermediate calculations. This material is available free of charge via the Internet at http://pubs.acs.org.

■ AUTHOR INFORMATION

Corresponding Author
*E-mail: scott.trammell@nrl.navy.mil. Phone: (202) 404-6063. Fax: (202) 767-9594.

■ ACKNOWLEDGMENT

■ REFERENCES

(1) Skourtis, S. S.; Waldeck, D. H.; Beratan, D. N. *Annu. Rev. Phys. Chem.* **2010**, *61*, 461–485.

(2) Beaujuge, P. M.; Amb, C. M.; Reynolds, J. R. *Acc. Chem. Res.* **2010**, *43*, 1396–1407.

(3) Yudanov, V. V.; Mikhailova, V. A.; Ivanov, A. I. *J. Phys. Chem. A* **2010**, *114*, 12998–13004.

(4) Verhoeven, J. W.; van Ramesdonk, H. J.; Groeneveld, M. M.; Benniston, A. C.; Harriman, A. *ChemPhysChem* **2005**, *6*, 2251–2260.

(5) Rosokha, S. V.; Kochi, J. K. *Acc. Chem. Res.* **2008**, *41*, 641–653.

(6) Soler, M.; McCusker, J. K. *J. Am. Chem. Soc.* **2008**, *130*, 4708–4724.

(7) Albinsson, B.; Eng, M. P.; Pettersson, K.; Winters, M. U. *Chem. Phys. Phys. Chem.* **2007**, *9*, 5847–5864.

(8) Newton, M. D. *Adv. Chem. Phys.* **1999**, *106*, 303–375.

(9) Stenuit, B. A.; Agathos, S. N. *Appl. Microbiol. Biotechnol.* **2010**, *88*, 1043–1064.

(10) Keiluweit, M.; Kleber, M. *Environ. Sci. Technol.* **2009**, *43*, 3421–3429.

(11) Chuzel, O.; Magnier-Bouvier, C.; Schulz, E. *Tetrahedron: Asymmetry* **2008**, *19*, 1010–1019.

(12) Rathore, R.; Kochi, J. K. *Adv. Phys. Org. Chem.* **2000**, *35*, 193–318.

(13) Forlani, L. *J. Phys. Org. Chem.* **1999**, *12*, 417–424.

(14) Bockman, T. M.; Kochi, J. K. *J. Phys. Org. Chem.* **1994**, *7*, 325–351.

(15) Takahashi, E.; Takaya, H.; Naota, T. *Chem.—Eur. J.* **2010**, *16*, 4793–4802.

(16) Sharon, E.; Freeman, R.; Willner, I. *Electroanalysis* **2009**, *21*, 2185–2189.

(17) Wang, H.; Lin, J. M.; Huang, W.; Wei, W. *Sens. Actuators B: Chem.* **2010**, *150*, 798–805.

(18) Binda, M.; Natali, D.; Sampietro, M.; Agostinelli, T.; Beverina, L. *Nucl. Instrum. Methods Phys. Res. A* **2010**, *624*, 443–448.

(19) Xing, Y. J.; Lin, H. Y.; Wang, F.; Lu, P. *Sens. Actuators B: Chem.* **2006**, *114*, 28–31.

(20) Fan, C. H.; Plaxco, K. W.; Heeger, A. J. *Trends Biotechnol.* **2005**, *23*, 186–192.

(21) Huang, J. H.; Wen, W. H.; Sun, Y. Y.; Chou, P. T.; Fang, J. M. *J. Org. Chem.* **2005**, *70*, 5827–5832.

(22) Baxter, P. N. W. *J. Org. Chem.* **2004**, *69*, 1813–1821.

(23) Olson, M. A.; Braunschweig, A. B.; Ikeda, T.; Fang, L.; Trabolsi, A.; Slawin, A. M. Z.; Khan, S. I.; Stoddart, J. F. *Org. Biomol. Chem.* **2009**, *7*, 4391–4405.

(24) Li, D.; Paxton, W. F.; Baughman, R. H.; Huang, T. J.; Stoddart, J. F.; Weiss, P. S. *MRS Bull.* **2009**, *34*, 671–681.

(25) D'Souza, F.; Chitta, R.; Gadde, S.; Zandler, M. E.; McCarty, A. L.; Sandanavska, A. S. D.; Araki, Y.; Ito, O. *J. Phys. Chem. A* **2006**, *110*, 4338–4347.

(26) Kato, T.; Yasuda, T.; Kamikawa, Y.; Yoshio, M. *Chem. Commun* **2009**, 729–739.

(27) Raymo, F. M.; Tomasulo, M. *Chem. Soc. Rev.* **2005**, *34*, 327–336.

(28) Akpinar, H.; Balan, A.; Baran, D.; Unver, E. K.; Toppare, L. *Polymer* **2010**, *51*, 6123–6131.

(29) Ikeda, T.; Stoddart, J. F. *Sci. Technol. Adv. Mater.* **2008**, *9*, 014104.

(30) Burattini, S.; Greenland, B. W.; Hayes, W.; Mackay, M. E.; Rowan, S. J.; Colquhoun, H. M. *Chem. Mater.* **2011**, *23*, 6–8.

(31) Balogh, D.; Tel-Vered, R.; Riskin, M.; Orbach, R.; Willner, I. *ACS Nano* **2011**, *5*, 299–306.

(32) Neue, U. D. *J. Sep. Sci.* **2007**, *30*, 1611–1627.

(33) Qian, G.; Wang, Z. Y. *Chem. Asian J.* **2010**, *5*, 1006–1029.

(34) Jiang, H. *Macromol. Rapid Commun.* **2010**, *31*, 2007–2034.

(35) Heeger, A. J. *Chem. Soc. Rev.* **2010**, *39*, 2354–2371.

(36) Zotti, G.; Vercelli, B.; Berlin, A. *Acc. Chem. Res.* **2008**, *41*, 1098–1109.

13460

dx.doi.org/10.1021/jp2023988 |*J. Phys. Chem. C* 2011, 115, 13446–13461

(37) Horiuchi, S.; Hasegawa, T.; Tokura, Y. *J. Phys. Soc. Jpn.* **2006**, *75*, 051016.

(38) Segalman, R. A.; McCulloch, B.; Kirmayer, S.; Urban, J. J. *Macromolecules* **2009**, *42*, 9205–9216.

(39) Yi, Y. P.; Zhu, L. Y.; Shuai, Z. G. *Macromol. Theory Simul.* **2008**, *17*, 12–22.

(40) Koch, N. *ChemPhysChem* **2007**, *8*, 1438–1455.

(41) Wolff, J. J.; Wortmann, R. *Adv. Phys. Org. Chem.* **1999**, *32*, 121–217.

(42) Zheng, Y.; Xue, J. G. *Polym. Rev.* **2010**, *50*, 420–453.

(43) Helgesen, M.; Sondergaard, R.; Krebs, F. C. *J. Mater. Chem.* **2010**, *20*, 36–60.

(44) Bredas, J.-L.; Norton, J. E.; Cornil, J.; Coropceanu, V. *Acc. Chem. Res.* **2009**, *42*, 1691–1699.

(45) Günes, S.; Neugebauer, H.; Sariciftci, N. S. *Chem. Rev.* **2007**, *107*, 1324–1338.

(46) Nelson, J. *Curr. Opin. Solid State Mater. Sci.* **2002**, *6*, 87–95.

(47) Hizume, Y.; Tashiro, K.; Charvet, R.; Yamamoto, Y.; Saeki, A.; Seki, S.; Aida, T. *J. Am. Chem. Soc.* **2010**, *132*, 6628–6629.

(48) Che, Y.; Yang, X.; Liu, G.; Yu, C.; Ji, H.; Zuo, J.; Zhao, J.; Zang, L. *J. Am. Chem. Soc.* **2010**, *132*, 5743–5750.

(49) Yamamoto, Y.; Zhang, G.; Jin, W.; Fukushima, T.; Ishii, N.; Saeki, A.; Seki, S.; Tagawa, S.; Minari, T.; Tsukagoshi, K.; Aida, T. *Proc. Natl. Acad. Sci. U.S.A.* **2009**, *106*, 21051–21056.

(50) Zhu, X.-Y.; Yang, Q.; Muntwiler, M. *Acc. Chem. Res.* **2009**, *42*, 1779–1787.

(51) Yan, H.; Swaraj, S.; Wang, C.; Hwang, I.; Greenham, N. C.; Groves, C.; Ade, H.; McNeill, C. R. *Adv. Funct. Mater.* **2010**, *20*, 4329–4337.

(52) van Bavel, S.; Veenstra, S.; Loos, J. *Macromol. Rapid Commun.* **2010**, *31*, 1835–1845.

(53) Youngblood, W. J.; Lee, S.-H. A.; Maeda, K.; Mallouk, T. E. *Acc. Chem. Res.* **2009**, *42*, 1966–1973.

(54) Otruba, J. P.; Neyhart, G. A.; Dressick, W. J.; Marshall, J. L.; Sullivan, B. P.; Watkins, P. A.; Meyer, T. J. *J. Photochem.* **1986**, *35*, 133–153.

(55) Cano-Yelo, H.; DeRonzier, A. *J. Chem. Soc., Faraday Trans. 1* **1984**, *80*, 3011–3019.

(56) Roncel, M.; Navarro, J. A.; De La Rosa, F. F.; De La Rosa, M. A. *Photochem. Photobiol.* **1984**, *40*, 395–398.

(57) Dressick, W. J.; Meyer, T. J.; Durham, B. *Isr. J. Chem.* **1982**, *22*, 153–157.

(58) Dressick, W. J.; Meyer, T. J.; Durham, B.; Rillema, D. P. *Inorg. Chem.* **1982**, *21*, 3451–3458.

(59) Neyhart, G. A.; Marshall, J. L.; Dressick, W. J.; Sullivan, B. P.; Watkins, P. A.; Meyer, T. J. *Chem. Commun.* **1982**, 915–917.

(60) Sullivan, B. P.; Dressick, W. J.; Meyer, T. J. *J. Phys. Chem.* **1982**, *86*, 1473–1478.

(61) Neumann-Spallart, M.; Kalyanasundaram, K. *Chem. Commun.* **1981**, 437–440.

(62) Neumann-Spallart, M.; Kalyanasundaram, K. *Ber. Bunsen-Ges. Phys. Chem.* **1981**, *85*, 704–709.

(63) Rillema, D. P.; Dressick, W. J.; Meyer, T. J. *Chem. Commun.* **1980**, 247–248.

(64) Neumann-Spallart, M.; Kalyanasundaram, K.; Grätzel, C.; Grätzel, M. *Helv. Chim. Acta* **1980**, *80*, 1111–1118.

(65) Durham, B.; Dressick, W. J.; Meyer, T. J. *Chem. Commun.* **1979**, 381–382.

(66) Hauenstein, B. L.; Dressick, W. J.; Demas, J. N.; Degraff, B. A. *J. Phys. Chem.* **1984**, *88*, 2418–2422.

(67) Dressick, W. J.; Hauenstein, B. L.; Demas, J. N.; Degraff, B. A. *Inorg. Chem.* **1984**, *23*, 1107–1113.

(68) Kepley, L. J.; Bard, A. J. *J. Electrochem. Soc.* **1995**, *142*, 4129–4138.

(69) Bookbinder, D. C.; Wrighton, M. S. *J. Electrochem. Soc.* **1983**, *130*, 1080–1087.

(70) Bruce, J. A.; Wrighton, M. S. *J. Am. Chem. Soc.* **1982**, *104*, 74–82.

(71) Álvaro, M.; Ferrer, B.; Fornés, V.; García, H. *Chem. Commun.* **2001**, 2546–2547.

(72) Braddock, J. N.; Meyer, T. J. *J. Am. Chem. Soc.* **1973**, *95*, 3158–3162.

(73) Huang, L.; Seward, K. J.; Sullivan, B. P.; Jones, W. E.; Mecholsky, J. J.; Dressick, W. J. *Inorg. Chim. Acta* **2000**, *310*, 227–236.

(74) Zanarini, S.; Della Ciana, L.; Marcaccio, M.; Marzocchi, E.; Paolucci, F.; Prodi, L. *J. Phys. Chem. B* **2008**, *112*, 10188–10193.

(75) Della Ciana, L.; Dressick, W. J.; Sandrini, D.; Maestri, M.; Ciano, M. *Inorg. Chem.* **1990**, *29*, 2792–2798.

(76) Launikonis, A.; Lay, P. A.; Mau, A. W.-H.; Sargeson, A. M.; Sasse, W. H. F. *Aust. J. Chem.* **1986**, *39*, 1053–1062.

(77) Della Ciana, L.; Dressick, W. J.; von Zelewsky, A. *J. Heterocyclic Chem.* **1990**, *27*, 163–165.

(78) Anderson, S.; Constable, E. C.; Seddon, K. R.; Turp, J. E.; Baggott, J. E.; Pilling, M. J. *J. Chem. Soc., Dalton Trans.* **1985**, 2247–2261.

(79) Moody, G. J.; Owusu, R. K.; Slawin, A. M. Z.; Spencer, N.; Stoddart, J. F.; Thomas, J. D. R.; Williams, D. J. *Angew. Chem. Int. Ed. Engl.* **1987**, *26*, 890–892.

(80) Babel, D.; Witzel, M. *Z. Krystallogr.* **1983**, *162*, 10–11.

(81) Gobetto, R.; Nervi, C.; Romanin, B.; Salassa, L.; Milanesio, M.; Croce, G. *Organometallics* **2003**, *22*, 4012–4019.

(82) Cotton, F. A.; Reid, A. H. *J. Acta Crystallogr. C* **1985**, *41*, 686–688.

(83) Dressick, W. J.; Dulcey, C. S.; Brandow, S. L.; Witschi, H.; Neeley, P. F. *J. Vac. Sci. Technol. A* **1999**, *17*, 1432–1440.

(84) Dressick, W. J.; Kondracki, L. M.; Chen, M.-S.; Brandow, S. L.; Matijević, E.; Calvert, J. M. *Colloids Surf. A* **1996**, *108*, 101–111.

(85) Wegner, E. E.; Adamson, A. W. *J. Am. Chem. Soc.* **1966**, *80*, 394–404.

(86) Box, G. E. P.; Hunter, W. G.; Hunter, J. S. *Statistics for Experimenters: An Introduction to Design, Data Analysis, and Model Building*; John Wiley & Sons Inc.: New York, 1978.

(87) Schmidt, S. R.; Launsby, R. G. *Understanding Industrial Designed Experiments*, 3rd ed.; Air Academy Press: Colorado Springs, CO, 1992.

(88) Dinderman, M. A.; Dressick, W. J.; Kostelansky, C. N.; Price, R. R.; Qadri, S. B.; Schoen, P. S. *Chem. Mater.* **2006**, *18*, 4361–4368.

(89) Dalton, E. F.; Murray, R. W. *J. Phys. Chem.* **1991**, *95*, 6383–6389.

(90) Raymo, F. M.; Alvarado, R. *J. Chem. Record* **2004**, *4*, 204–218.

(91) Deepa, P. N.; Kanungo, M.; Claycomb, G.; Sherwood, P. M. A.; Collinson, M. M. *Anal. Chem.* **2003**, *75*, 5399–5405.

(92) Laidler, K. J. *Chemical Kinetics*, 3rd ed.; Harper & Row: New York, 1987.

(93) Ito, F.; Nagamura, T. *J. Photochem. Photobiol. C: Photochem. Rev.* **2007**, *8*, 174–190.

(94) Schindler, P.; Kamber, H. R. *Helv. Chim. Acta* **1968**, *51*, 1781–1786.

(95) Iler, R. K. *The Chemistry of Silica: Soubility, Polymerization, Colloid and Surface Properties, and Biochemistry*; John Wiley & Sons Inc.: New York, 1979.

(96) Collins, K. D. *Biophys. Chem.* **2006**, *119*, 271–281.

(97) Jenkins, H. D. B. *Chem. Rev.* **1995**, *95*, 2695–2724.

(98) *CRC Handbook of Chemistry & Physics*, 78th ed.; Lide, D. R., Ed.; CRC Press: Boca Raton, FL, 1997.

(99) Schiavo, S.; Fuoss, R. M.; Marrosu, G. *J. Solution Chem.* **1980**, *9*, 563–581.

Supplementary Information

Photocurrents from the Direct Irradiation of a Donor-Acceptor Complex Contained
in a Thin Film on Indium Tin Oxide

Scott A. Trammell*, Walter J. Dressick, Brian J. Melde, and Martin Moore

Naval Research Laboratory

Center for Bio/Molecular Science & Engineering (Code 6900)

4555 Overlook Avenue, SW

Washington, DC 20375

*Contact Information:

E-mail: scott.trammell@nrl.navy.mil

Phone: (202) 404-6043

Fax: (202) 767-9594

This supplementary information is organized in two sections describing film porosity measurements and statistical calculations, respectively.

Section 1

This section provides an illustration of the structures of the redox probes used to investigate changes in **PQS** film porosity with film aging in Figure S-1. A summary of the currents obtained from cyclic voltammetry studies of the redox probes using 3 day old and 7 day old **PQS** film electrodes is shown in Table S-1.

Section 2

This section briefly describes the statistical calculations associated with the two-level factorial design experiments and provides appropriate data and calculation summaries in tabular form that complement the discussion in the main text. For a more complete discussion of the statistical methods used to make the calculations, the reader is referred to the literature references.[S-1, S-2] Table S-2 lists the measured photocurrents (i_P) for solutions containing $NaBPh_4$ and background (i_B) photocurrents for analogous blank solutions not containing $NaBPh_4$ for each experiment summarized in Table 1 of the main text. Experiments are designated by the row number in column 1 and identified by the levels of the coded variables in the factorial design matrix summarized in columns 2-6 of Table S-2. Therefore, each row in Table S-2 describes the parameters and results for a specific experiment defined by the values of the (**L**), (**F**), (**C**), (**P**), and (**A**) variables. Although listed in numerical order for convenient identification, experiments were performed in random order as shown in Table 1 in the main text. Photocurrent values corresponding to three individual measurements are shown in order of measurement for each of the i_P

and i_B in row (experiment) in Table S-2. Additional information regarding solution compositions

and experimental conditions is listed in the Experimental Section and Table 1 in the main text.

Table S-3 summarizes the statistical parameters calculated for the i_P and i_B. Because n =

3 measurements were made in each experiment for each of the i_P and i_B, there are n − 1 = 2 de-

grees of freedom, DF, for each of the i_P and i_B measurements. Average photocurrents are sepa-

rately calculated for the i_P and i_B in each row of Table S-3 using equation (S-1):

$$\text{Ave. } i_X = \tfrac{1}{3} \cdot \Sigma_{j=1\text{-}3} (i_{X,j}) \qquad (X = P, B) \qquad \text{(S-1)}$$

The sum of the squares of the deviations of the measured photocurrents, $i_{X,j}$, from the average

photocurrent, Ave. i_X, is designated by S_X and is calculated for the i_P and i_B from each row in

Table S-3 by equation (S-2):

$$S_X = \Sigma_{j=1\text{-}3} \left[(i_{X,j}) - (\text{Ave. } i_X) \right]^2 \qquad (X = P, B) \qquad \text{(S-2)}$$

The sample variances, designated $SV(i_X)$, are calculated from the S_X and DF using equation (S-3):

$$SV(i_X) = S_X / DF \qquad (X = P, B) \qquad \text{(S-3)}$$

Finally, because the background photocurrent, i_B, originates from the ITO electrode, it is present

as a component of the photocurrent measured in the presence of $NaBPh_4$, i_P. Therefore, it is also

necessary to calculate the covariance, $Cov(i_P, i_B)$, of the i_P, i_B pairs in each row of Table S-3 us-

ing equation (S-4):

$$Cov(i_P, i_B) = \tfrac{1}{3} \cdot \Sigma_{j=1\text{-}3} \left[(i_{P,j}) \cdot (i_{B,j}) \right] - (\text{Ave. } i_P) \cdot (\text{Ave. } i_B) \qquad \text{(S-4)}$$

Table S-4 summarizes the calculation of the average of the net measured photocurrent, i_N, and its sample variance, $SV(i_N)$, using the information listed in Table S-3. The i_N are calculated as the difference between the Ave. i_P and Ave. i_B for each experiment according to equation (S-5):

$$\text{Ave. } i_N = \text{Ave. } i_P - \text{Ave. } i_B \tag{S-5}$$

The $SV(i_N)$ are calculated from the $SV(i_P)$, $SV(i_B)$, and $Cov(i_P, i_B)$ in Table S-3 according to equation (S-6):

$$SV(i_N) = SV(i_P) + SV(i_B) - 2 \cdot Cov(i_P, i_B) \tag{S-6}$$

The mean square error of the measurements (MSE) required for the analysis of variance (ANOVA) calculations is also calculated from the information in Table S-4 using equation (S-7):

$$Y = \Sigma_{j = 1\text{-}32} \, [(DF_j) \cdot (SV(i_N)_j)] = 4472.44 \tag{S-7a}$$

$$Z = \Sigma_{j = 1\text{-}32} \, (DF_j) = 32 \tag{S-7b}$$

$$MSE = Y \, / \, Z = 139.765 \tag{S-7c}$$

The summations in equations (S-7) are taken over the j = 1 to 32 rows in Table S-4.

Table S-5 summarizes the calculations of the effects, E (nA), due to each variable or combination of variables, on the i_N using the Ave. i_N from Table S-4 and Yates' Algorithm.[S-1] The grand average (GA) photocurrent obtained from the factorial design, $GA(i_N) = 172.8667$ nA, appears in the first row of the effects column, with the remaining column entries represent the effects due to each variable or combination of variables, as identified in the column labeled "ID",

on the i_N. Entries in the columns labeled "Col." represent intermediate calculation values generated during the Yates' Algorithm calculations.

Table S-6 summarizes the ANOVA calculations using the effects listed in Table S-5 and the MSE calculated from Table S-4. For a detailed discussion concerning the hypothesis testing methods comprising the ANOVA calculations, the reader is referred to the literature.[S-2] In order to determine whether an effect is statistically significant, the mean square error between (variable) levels (MSB) is first calculated for each effect. For a two-level factorial design, MSB is defined by equation (S-8), where $N = 32$ is the total number of i_N:

$$MSB = N \cdot E^2 / 4 = 8 \cdot E^2 \qquad (S-8)$$

An F-distribution value, F_0, is then calculated for each effect using the MSB and MSE according to equation (S-9):

$$F_0 = MSB / MSE \qquad (S-9)$$

In order to determine whether the effect represented by F_0 is statistically significant, F_0 is compared to the appropriate $F_c(1-\alpha, DF_{MSB}, DF_{MSE})$ value in an F-distribution table.[S-2] For our work, we have selected $\alpha = 0.001$ (*i.e.*, 0.999 confidence level) for evaluation of our results. For our two-level factorial design, the degrees of freedom associated with the MSB is one less than the number of design levels by definition, so that $DF_{MSB} = 2 - 1 = 1$.[S-2] The degrees of freedom for the MSE, DF_{MSE}, is defined by equation (S-7b) with $DF_{MSE} = Z = 32$. Therefore, the value $F_c(0.999, 1, 32)$ is required. Because a value for $F_c(0.999, 1, 32)$ is not listed in the F-distribution table, we use the next nearest more conservative value listed of $F_c(0.999, 1, 30) = 13.3$. For the ratios of $F_0/F_c \leq 1$ listed in Table S-6, the corresponding effects are judged not sta-

tistically significant and are attributed to random error. These are indicated by an entry of "No" in the column labeled "Significance". Ratios of $F_0/F_c > 1$ signify that the effect associated with that specific variable or combinations of variables is statistically significant. These are indicated by an entry of "Yes" in the "Significance" column.

Table S-7 summarizes the parameters used to prepare the normal probability plot shown in Figure 4 in the main text. Effects are shown listed in increasing order from smallest to largest. Corresponding cumulative probability values, P_j, associated with each effect are calculated from equation (S-10) for each of the $j = 31$ effects:

$$P_j = 100 \cdot (j - \tfrac{1}{2}) / 31 \qquad\qquad (S\text{-}10)$$

Calculations associated with use of model equation 9 (note main article text) to estimate the i_N values at each of the various ±1 level combinations of the variables from the statistically significant effects are summarized in Table S-8. Under these circumstances, the Reverse Yates' Algorithm[S-1] provides a more convenient means than equation 9 to make the necessary calculations and is therefore used here. The calculation uses Col. 5 values in inverted order from the Yates' Algorithm calculation of Table S-5 in which entries corresponding to effects deemed not statistically significant (*i.e.*, S = "No") via the ANOVA results of Table S-6 are set to zero. The numbers listed in the columns labeled "Reverse Col." are intermediate values associated with the Reverse Yates' Algorithm calculations. The photocurrents calculated from the statistically significant effects are listed for each row in the column labeled "i_N Estimated".

The "i_N Estimated" values derived in Table S-8 are used to calculate the residuals, Δi_N, listed in Table S-9, which represent the differences between the predicted i_N obtained for the model from the Reverse Yates' Algorithm calculations and the corresponding measured "Ave. i_N" from Table S-4. Note that the order of the "Ave i_N" in Table S-9 is the inverse of that in Ta-

ble S-4 to correspond with the results for the "i_N Estimated" values from Table S-8. The residuals are calculated for each row in Table S-9 from equation (S-11):

$$\Delta i_N = (i_N \text{ Estimated}) - (\text{Ave } i_N) \qquad\qquad (S\text{-}11)$$

Residuals are summarized in column 3 of Table S-9.

Table S-10 summarizes the parameters used to prepare the residuals plot shown in Figure 6 in the main text. Residuals taken from Table S-9 are shown separately listed in increasing order from smallest to largest. Corresponding cumulative probability values, P_j, associated with each residual are calculated from equation (S-12) for each of the $j = 32$ experiments:

$$P_j = 100 \cdot (j - \frac{1}{2}) / 32 \qquad\qquad (S\text{-}12)$$

Finally Tables S-11 and S-12 summarize the data and calculations of the average i_N for cells operating using the bromide and nitrate electrolyte solutions discussed in connection with Table 2 in the main article text. The calculations in Table S-12 are performed as described for Tables S-3 and S-4. Additional information and details related to the information described in Sections 1 and 2 are presented in the discussion in the main article text.

References:

S-1.   Box, G.E.P.; Hunter, W.G.; Hunter, J.S. *Statistics for Experimenters: An Introduction to Design, Data Analysis, and Model Building*, John Wiley & Sons Inc.: New York, NY, **1978**; Ch. 10.

S-2.   Schmidt; S.R.; Launsby, R.G., *Understanding Industrial Designed Experiments, 3rd Ed.*, Air Academy Press: Colorado Springs, CO, **1992**; Ch. 4-5.

S-3.   Babel, D.; Witzel, M., *Z. Kristallogr*. **1983**, *162*, 10-11.

S-4.   Gobetto, R.; Nervi, C.; Romanin, B.; Salassa, L.; Milanesio, M.; Croce, G., *Or-ganometallics* **2003**, *22*, 4012-4019.

S-5.   Cotton, F.A.; Reid, A.H.J., *Acta Cryst. Sec. C* **1985**, *41*, 686-688.

$Na_4Ru(BPS)_3$ (2.10 nm)

$Na_4Ru(DCbpy)_3$ (1.34 nm)

$(Cp)Fe(Cp)COOH$ (0.46 nm)

$Ru(bpy)_3(ClO_4)_2$ (1.16 nm)

$(bpy)_2Os(CO)Cl(ClO_4)$ (0.96 nm)

$Na_4Fe(CN)_6$ (0.61 nm)
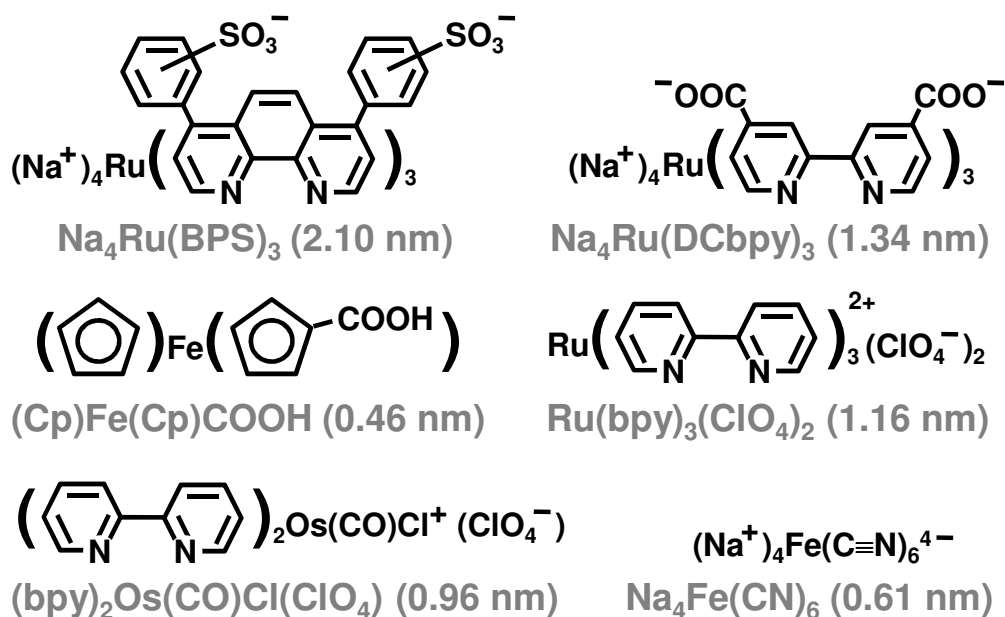
Figure S-1: Structures of redox probes. Values in parentheses represent the diameter of each species calculated from the radius. The radii of the complexes $Na_4Fe(CN)_6$,[S-3] $Ru(bpy)_3ClO_4$,[S-3] $(bpy)_2Os(CO)Cl(ClO_4)$[S-4], $CpFeCpCOOH$[S-5] were taken as the geometric average of the maximum radial length and its two orthogonal radial lengths from X-ray crystal structure data. For $Na_4Ru(BPS)_3$ and $Na_4Ru(DCbpy)_3$, an energy minimized structure was calculated using the ACD/3D Viewer in the ChemSketch® program from Advanced Chemistry Development, Inc.

Table S-1: Current Measurements for the Redox Probes of Figure S-1 in **PQS** Films

Material[a]	Size[b]	i(μA)[c, d] (A) = −1	i(μA)[c, e] (A) = +1
Na$_4$Ru(BPS)$_3$	2.10 nm	1.8	1
Na$_4$Ru(DCbpy)$_3$	1.34 nm	109	104
Ru(bpy)$_3$(ClO$_4$)$_2$	1.16 nm	7	7
(bpy)$_2$Os(CO)Cl(ClO$_4$)	0.96 nm	21	19
Na$_4$Fe(CN)$_6$	0.61 nm	54	56
CpFeCpCOOH	0.46 nm	37	36

[a] Structure shown in Figure S-1.

[b] Diameter calculated as described in Figure S-1.

[c] Anodic (i$_a$) current from the cyclic voltammogram corresponding to the oxidation of the redox probe. Voltammograms were obtained at room temperature (22 ± 2°C) in an aerated 100 mM NaCl (aq) solution containing 500 μM redox probe at a scan rate of 100 mV·s^{-1} using the **PQS** film ITO electrode as the working electrode with a Ag/AgCl reference electrode and Pt wire counter electrode.

[d] Working electrode is a 3 day old **PQS** film on ITO electrode.

[e] Working electrode is a 7 day old **PQS** film on ITO electrode.

Table S-2: Photocurrent Data

Row[a]	L[b]	F[b]	C[b]	P[b]	A[b]	i_P (nA)[c]			i_B (nA)[d]		
1	−1	−1	−1	−1	−1	66	61	63	4.7	4.5	4.4
2	+1	−1	−1	−1	−1	229	226	221	12	11.7	12
3	−1	+1	−1	−1	−1	80	80	77	4.7	4.5	4.4
4	+1	+1	−1	−1	−1	279	274	252	12	11.7	12
5	−1	−1	+1	−1	−1	45	45	44	4.4	4.5	4.7
6	+1	−1	+1	−1	−1	149	150	148	9.2	8.8	9
7	−1	+1	+1	−1	−1	58	53	55	4.4	4.5	4.7
8	+1	+1	+1	−1	−1	187	188	184	9.2	8.8	9
9	−1	−1	−1	+1	−1	160	154	152	3.5	3.2	3.4
10	+1	−1	−1	+1	−1	600	588	573	13.4	12.9	12.7
11	−1	+1	−1	+1	−1	213	207	202	3.5	3.2	3.4
12	+1	+1	−1	+1	−1	556	533	524	13.4	12.9	12.7
13	−1	−1	+1	+1	−1	108	107	104	3	3	3
14	+1	−1	+1	+1	−1	472	460	448	9.6	9.2	9.1
15	−1	+1	+1	+1	−1	120	120	120	3	3	3
16	+1	+1	+1	+1	−1	476	459	450	9.6	9.2	9.1
17	−1	−1	−1	−1	+1	77	73	71	23	23	22
18	+1	−1	−1	−1	+1	242	241	223	110	103	100
19	−1	+1	−1	−1	+1	80	84	77	23	23	22
20	+1	+1	−1	−1	+1	272	267	255	110	103	100
21	−1	−1	+1	−1	+1	47	46	45	22	22	21
22	+1	−1	+1	−1	+1	205	192	183	59	56	53
23	−1	+1	+1	−1	+1	58	58	55	22	22	21
24	+1	+1	+1	−1	+1	247	226	215	59	56	53
25	−1	−1	−1	+1	+1	152	148	146	60	57	55
26	+1	−1	−1	+1	+1	492	461	444	222	213	208
27	−1	+1	−1	+1	+1	75	74	75	60	57	55
28	+1	+1	−1	+1	+1	490	467	400	222	213	208
29	−1	−1	+1	+1	+1	119	116	110	65	64	64
30	+1	−1	+1	+1	+1	396	374	360	189	183	180
31	−1	+1	+1	+1	+1	144	138	135	65	64	64
32	+1	+1	+1	+1	+1	465	437	418	189	183	180

[a] Experiment number designation.
[b] Coded variables as defined in Table 1 and the main text in the article.
[c] Measured photocurrents in solutions containing $NaBPh_4$.
[d] Measured photocurrents in blank solutions not containing $NaBPh_4$.

Table S-3: Photocurrent Averages and Sample Variances

Row[a]	DF[b]	Ave. i_P[c]	S_P[d]	SV(i_P)[e]	Ave. i_B[f]	S_B[g]	SV(i_B)[h]	Cov(i_P, i_B)[i]
1	2	63.33333	12.66667	6.333333	4.533333	0.046667	0.023333	0.188889
2	2	225.3333	32.66667	16.33333	11.9	0.06	0.03	−0.06667
3	2	79	6	3	4.533333	0.046667	0.023333	0.133333
4	2	268.3333	412.6667	206.3333	11.9	0.06	0.03	−0.56667
5	2	44.66667	0.666667	0.333333	4.533333	0.046667	0.023333	−0.05556
6	2	149	2	1	9	0.08	0.04	−0.06667
7	2	55.33333	12.66667	6.333333	4.533333	0.046667	0.023333	−0.11111
8	2	186.3333	8.666667	4.333333	9	0.08	0.04	−0.06667
9	2	155.3333	34.66667	17.33333	3.366667	0.046667	0.023333	0.244444
10	2	587	366	183	13	0.26	0.13	3.1
11	2	207.3333	60.66667	30.33333	3.366667	0.046667	0.023333	0.211111
12	2	537.6667	544.6667	272.3333	13	0.26	0.13	3.966667
13	2	106.3333	8.666667	4.333333	3	0	0	0
14	2	460	288	144	9.3	0.14	0.07	2
15	2	120	0	0	3	0	0	0
16	2	461.6667	348.6667	174.3333	9.3	0.14	0.07	2.3
17	2	73.66667	18.66667	9.333333	22.66667	0.666667	0.333333	0.888889
18	2	235.3333	228.6667	114.3333	104.3333	52.66667	26.33333	27.88889
19	2	80.33333	24.66667	12.33333	22.66667	0.666667	0.333333	1.111111
20	2	264.6667	152.6667	76.33333	104.3333	52.66667	26.33333	26.77778
21	2	46	2	1	21.66667	0.666667	0.333333	0.333333
22	2	193.3333	244.6667	122.3333	56	18	9	22
23	2	57	6	3	21.66667	0.666667	0.333333	0.666667
24	2	229.3333	528.6667	264.3333	56	18	9	32
25	2	148.6667	18.66667	9.333333	57.33333	12.66667	6.333333	5.111111
26	2	465.6667	1184.667	592.3333	214.3333	100.6667	50.33333	115.1111
27	2	74.66667	0.666667	0.333333	57.33333	12.66667	6.333333	0.111111
28	2	452.3333	4372.667	2186.333	214.3333	100.6667	50.33333	200.2222
29	2	115	42	21	64.33333	0.666667	0.333333	1.333333
30	2	376.6667	658.6667	329.3333	184	42	21	55.33333
31	2	139	42	21	64.33333	0.666667	0.333333	1.666667
32	2	440	1118	559	184	42	21	72

[a] Experiment number designation.

[b] Degrees of freedom.

[c] Average i_p (nA) calculated from individual i_p values in the corresponding row of Table S-2.

[d] Sum of the squares of the deviations of the individual i_P values in the corresponding row of Table S-2 from the average i_P value.

[e] Sample variance for the i_P.

[f] Average i_B (nA) calculated from individual i_B values in the corresponding row of Table S-2.

[g] Sum of the squares of the deviations of the individual i_B values in the corresponding row of Table S-2 from the average i_B value.

[h] Sample variance for the i_B.

[i] Sample covariance for the paired i_P, i_B measurements.

Table S-4: Net Photocurrent Values and Statistical Parameters

Row[a]	Ave. i_N (nA)[b]	SV(i_N)[c]	DF[d]
1	58.8	5.978889	1
2	213.4333	16.49667	1
3	74.46667	2.756667	1
4	256.4333	207.4967	1
5	40.13333	0.467778	1
6	140	1.173333	1
7	50.8	6.578889	1
8	177.3333	4.506667	1
9	151.9667	16.86778	1
10	574	176.93	1
11	203.9667	29.93444	1
12	524.6667	264.53	1
13	103.3333	4.333333	1
14	450.7	140.07	1
15	117	0	1
16	452.3667	169.8033	1
17	51	7.888889	1
18	131	84.88889	1
19	57.66667	10.44444	1
20	160.3333	49.11111	1
21	24.33333	0.666667	1
22	137.3333	87.33333	1
23	35.33333	2	1
24	173.3333	209.3333	1
25	91.33333	5.444444	1
26	251.3333	412.4444	1
27	17.33333	6.444444	1
28	238	1836.222	1
29	50.66667	18.66667	1
30	192.6667	239.6667	1
31	74.66667	18	1
32	256	436	1

[a] Experiment number designation.

[b] Average i_N (nA) calculated from the difference between the average i_p and i_B values, $i_P - i_B$, in the corresponding row of Table S-3.

[c] Sample variance of the i_N calculated as the sum of the sample variances of the i_P and i_B minus twice the covariance of the measured i_P, i_B pair in the corresponding row of Table S-2.

[d] Degrees of freedom.

Table S-5: Determination of Effects Using Yates' Algorithm

Row[a]	i_N, (nA)[b]	Col. 1[c]	Col. 2[c]	Col. 3[c]	Col. 4[c]	Col. 5[c]	D[d]	Effect, E[e]	ID[f]
1	58.8	272.2333	603.1333	1011.4	3589.4	5531.733	32	172.8667	Average
2	213.4333	330.9	408.2667	2578	1942.333	3126.133	16	195.3833	L
3	74.46667	180.1333	1454.6	770.3333	1988.467	207.6667	16	12.97917	F
4	256.4333	228.1333	1123.4	1172	1137.667	88.33333	16	5.520833	LF
5	40.13333	725.9667	400	563	124.6667	−579.733	16	−36.2333	C
6	140	728.6333	370.3333	1425.467	83	−159.2	16	−9.95	LC
7	50.8	554.0333	598	433.6667	−59.3333	187.6667	16	11.72917	FC
8	177.3333	569.3667	574	704	147.6667	69.66667	16	4.354167	LFC
9	151.9667	182	336.6	106.6667	−526.067	1968.267	16	123.0167	P
10	574	218	226.4	18	−53.6667	1132.8	16	70.8	LP
11	203.9667	161.6667	742.7333	83	−170.2	−171.667	16	−10.7292	FP
12	524.6667	208.6667	682.7333	0	11	−115	16	−7.1875	LFP
13	103.3333	342.6667	182.6667	54	2	−130.667	16	−8.16667	CP
14	450.7	255.3333	251	−113.333	185.6667	−75.4667	16	−4.71667	LCP
15	117	243.3333	380.6667	47.66667	88.66667	187	16	11.6875	FCP
16	452.3667	330.6667	323.3333	100	−19	66.33333	16	4.145833	LFCP
17	51	154.6333	58.66667	−194.867	1566.6	−1647.07	16	−102.942	A
18	131	181.9667	48	−331.2	401.6667	−850.8	16	−53.175	LA
19	57.66667	99.86667	2.666667	−29.6667	862.4667	−41.6667	16	−2.60417	FA
20	160.3333	126.5333	15.33333	−24	270.3333	207	16	12.9375	LFA
21	24.33333	422.0333	36	−110.2	−88.6667	472.4	16	29.525	CA
22	137.3333	320.7	47	−60	−83	181.2	16	11.325	LCA
23	35.33333	347.3667	−87.3333	68.33333	−167.333	183.6667	16	11.47917	FCA
24	173.3333	335.3667	87.33333	−57.3333	52.33333	−107.667	16	−6.72917	LFCA
25	91.33333	80	27.33333	−10.6667	−136.333	−1164.93	16	−72.8083	PA
26	251.3333	102.6667	26.66667	12.66667	5.666667	−592.133	16	−37.0083	LPA
27	17.33333	113	−101.333	11	50.2	5.666667	16	0.354167	FPA
28	238	138	−12	174.6667	−125.667	219.6667	16	13.72917	LFPA
29	50.66667	160	22.66667	−0.66667	23.33333	142	16	8.875	CPA
30	192.6667	220.6667	25	89.33333	163.6667	−175.867	16	−10.9917	LCPA
31	74.66667	142	60.66667	2.333333	90	140.3333	16	8.770833	FCPA
32	256	181.3333	39.33333	−21.3333	−23.6667	−113.667	16	−7.10417	LFCPA

[a] Experiment number designation.

[b] Average i_N (nA) values from Table S-4 for each experiment.

[c] Values from intermediate calculations for the Yates' Algorithm.

[d] Divisor.

[e] Calculated effect for the variable or combination of variables listed shown in the same row of the column labeled "*ID*" on the measured net photocurrent, i_N.

[f] Identification of the variable or combination of variables attributed to each effect in the preceding column of the table.

Table S-6: ANOVA Parameters and Calculations

Row[a]	ID[b]	Effect, E[c]	MSB[d]	F_0[e]	F_0/F_c[f]	Significance, S[g]
1	Average	172.8667	–	–	–	–
2	L	195.3833	305397.2	2185.076	164.2914	Yes
3	F	12.97917	1347.67	9.642401	0.724993	No
4	LF	5.520833	243.8368	1.74462	0.131174	No
5	C	−36.2333	10502.84	75.14639	5.650105	Yes
6	LC	−9.95	792.02	5.666798	0.426075	No
7	FC	11.72917	1100.587	7.874552	0.592072	No
8	LFC	4.354167	151.6701	1.08518	0.081592	No
9	P	123.0167	121064.8	866.2026	65.12801	Yes
10	LP	70.8	40101.12	286.9182	21.5728	Yes
11	FP	−10.7292	920.9201	6.589061	0.495418	No
12	LFP	−7.1875	413.2813	2.956972	0.222329	No
13	CP	−8.16667	533.5556	3.817519	0.287032	No
14	LCP	−4.71667	177.9756	1.273391	0.095744	No
15	FCP	11.6875	1092.781	7.818705	0.587873	No
16	LFCP	4.145833	137.5035	0.983819	0.073971	No
17	A	−102.942	84775.89	606.5603	45.60603	Yes
18	LA	−53.175	22620.65	161.8477	12.169	Yes
19	FA	−2.60417	54.25347	0.388176	0.029186	No
20	LFA	12.9375	1339.031	9.580591	0.720345	No
21	CA	29.525	6973.805	49.89665	3.751628	Yes
22	LCA	11.325	1026.045	7.341216	0.551971	No
23	FCA	11.47917	1054.17	7.542447	0.567101	No
24	LFCA	−6.72917	362.2535	2.591875	0.194878	No
25	PA	−72.8083	42408.43	303.4267	22.81403	Yes
26	LPA	−37.0083	10956.93	78.39541	5.894391	Yes
27	FPA	0.354167	1.003472	0.00718	0.00054	No
28	LFPA	13.72917	1507.92	10.78897	0.811201	No
29	CPA	8.875	630.125	4.508461	0.338982	No
30	LCPA	−10.9917	966.5339	6.915422	0.519957	No
31	FCPA	8.770833	615.4201	4.403249	0.331071	No
32	LFCPA	−7.10417	403.7535	2.888802	0.217203	No

[a] Experiment number designation.

[b] Identification of variable(s) attributed to each effect in the same table row.

[c] Effect of the variable or combination of variables designated in the column labeled "**ID**" on i_N as determined by Yates' Algorithm analysis (note Supplementary Table S-5).

[d] Mean square error between levels (MSB) calculated as one-fourth of the product of the total number of i_N measured, N (=32), and the square of each effect, E, for the two-level factorial design.

[e] F-distribution value (*i.e.*, the MSB divided by the mean square error of the data, MSE (=139.765)).

[f] Significance ratio at the 0.999 confidence limit calculated using $F_c(0.999, 1, 30)$ as an estimate for $F_c(0.999, 1, 32)$ from the F-distribution table.[S-2]

[g] Significance (0.999 confidence level) determined by ANOVA. Designations: "No" ≡ Not statistically significant; "Yes" ≡ Significant.

Table S-7: Normal Probability Plot Information

Order (j)	Probability P_j[a]	Ordered Effect, E[b]	ID[c]
1	1.612903	−102.941667	A
2	4.83871	−72.8083333	PA
3	8.064516	−53.175	LA
4	11.29032	−37.0083333	LPA
5	14.51613	−36.2333333	C
6	17.74194	−10.9916667	LCPA
7	20.96774	−10.7291667	FP
8	24.19355	−9.95	LC
9	27.41935	−8.16666667	CP
10	30.64516	−7.1875	LFP
11	33.87097	−7.10416667	LFCPA
12	37.09677	−6.72916667	LFCA
13	40.32258	−4.71666667	LCP
14	43.54839	−2.60416667	FA
15	46.77419	0.35416667	FPA
16	50	4.14583333	LFCP
17	53.22581	4.35416667	LFC
18	56.45161	5.52083333	LF
19	59.67742	8.77083333	FCPA
20	62.90323	8.875	CPA
21	66.12903	11.325	LCA
22	69.35484	11.4791667	FCA
23	72.58065	11.6875	FCP
24	75.80645	11.7291667	FC
25	79.03226	12.9375	LFA
26	82.25806	12.9791667	F
27	85.48387	13.7291667	LFPA
28	88.70968	29.525	CA
29	91.93548	70.8	LP
30	95.16129	123.016667	P
31	98.3871	195.383333	L

[a] Cumulative probability of occurrence as defined by $P_j = 100(j − ½)/31$.

[b] Effect of the variable or combination of variables designated in the column labeled **ID** on i_N as determined by Yates' Algorithm analysis (note Table S-5).

[c] Identification of variable of combination of variables attributed to each effect in the preceding column of the table.

Table S-8: Reverse Yates' Algorithm for Estimation of Photocurrents

ID[a]	Modified Inverted Col. 5[b]	Reverse Col. 1[c]	Reverse Col. 2[c]	Reverse Col. 3[c]	Reverse Col. 4[c]	Reverse Col. 5[c]	D[d]	i_N (nA) Estimated[e]
LFCPA	0	0	0	−1757.06	−3782.53	7396.667	32	231.1458
FCPA	0	0	−1757.06	−2025.47	11179.2	1764.667	32	55.14584
LCPA	0	0	472.4	3101.067	−896.667	7396.667	32	231.1458
CPA	0	−1757.06	−2497.87	8078.133	2661.334	1764.667	32	55.14584
LFPA	0	0	0	−572.797	−3782.53	7611.333	32	237.8542
FPA	0	472.4	3101.067	−323.87	11179.2	1979.333	32	61.85416
LPA	−592.133	0	−579.733	835.467	−896.667	7611.333	32	237.8542
PA	−1164.93	−2497.87	8657.866	1825.867	2661.334	1979.333	32	61.85416
LFCA	0	0	0	−1757.06	−4727.33	4708.659	32	147.1456
FCA	0	0	−572.797	−2025.47	12338.67	1239.327	32	38.72897
LCA	0	0	472.4	3101.067	−1841.47	4708.659	32	147.1456
CA	472.4	3101.067	−796.27	8078.133	3820.8	1239.327	32	38.72897
LFA	0	0	0	−572.797	−4727.33	4923.325	32	153.8539
FA	0	−579.733	835.467	−323.87	12338.67	1453.993	32	45.43728
LA	−850.8	0	−579.733	835.467	−1841.47	4923.325	32	153.8539
A	−1647.07	8657.866	2405.6	1825.867	3820.8	1453.993	32	45.43728
LFCP	0	0	0	−1757.06	−268.407	14961.73	32	467.5542
FCP	0	0	−1757.06	−2970.27	4977.066	3558.001	32	111.1875
LCP	0	0	472.4	3101.067	248.927	14961.73	32	467.5542
CP	0	−572.797	−2497.87	9237.599	990.4	3558.001	32	111.1875
LFP	0	0	0	−572.797	−268.407	17066	32	533.3125
FP	0	472.4	3101.067	−1268.67	4977.066	5662.267	32	176.9458
LP	1132.8	0	−579.733	835.467	248.927	17066	32	533.3125
P	1968.267	−796.27	8657.866	2985.333	990.4	5662.267	32	176.9458
LFC	0	0	0	−1757.06	−1213.21	5245.473	32	163.921
FC	0	0	−572.797	−2970.27	6136.532	741.473	32	23.17103
LC	0	0	472.4	3101.067	−695.873	5245.473	32	163.921
C	−579.733	835.467	−796.27	9237.599	2149.866	741.473	32	23.17103
LF	0	0	0	−572.797	−1213.21	7349.739	32	229.6793
F	0	−579.733	835.467	−1268.67	6136.532	2845.739	32	88.92934
L	3126.133	0	−579.733	835.467	−695.873	7349.739	32	229.6793
Average	5531.733	2405.6	2405.6	2985.333	2149.866	2845.739	32	88.92934

[a] Identification of variable of combination of variables.

[b] Inverted column 5 from Yates's Algorithm calculations in Table S-5 with values for variables and variable combinations determined as not significant (S = "No") from the ANOVA calculation in Table S-6 set to zero.

[c] Values from intermediate calculations for the Reverse Yates' Algorithm.

[d] Divisor.

[e] Estimated i_N photocurrent values calculated from the system model derived from the factorial design using the Reverse Yates' Algorithm.

Table S-9: Residuals Calculations

i_N (nA) Estimated[a]	i_N (nA) Measured[b]	Residual Δi_N (nA)[c]
231.1458	256	24.85416
55.14584	74.66667	19.52082
231.1458	192.6667	−38.4792
55.14584	50.66667	−4.47918
237.8542	238	0.145844
61.85416	17.33333	−44.5208
237.8542	251.3333	13.47918
61.85416	91.33333	29.47918
147.1456	173.3333	26.18774
38.72897	35.33333	−3.39564
147.1456	137.3333	−9.81226
38.72897	24.33333	−14.3956
153.8539	160.3333	6.479427
45.43728	57.66667	12.22939
153.8539	131	−22.8539
45.43728	51	5.562719
467.5542	452.3667	−15.1875
111.1875	117	5.812469
467.5542	450.7	−16.8542
111.1875	103.3333	−7.8542
533.3125	524.6667	−8.6458
176.9458	203.9667	27.02082
533.3125	574	40.68753
176.9458	151.9667	−24.9792
163.921	177.3333	13.4123
23.17103	50.8	27.62897
163.921	140	−23.921
23.17103	40.13333	16.9623
229.6793	256.4333	26.75399
88.92934	74.46667	−14.4627
229.6793	213.4333	−16.246
88.92934	58.8	−30.1293

[a] Estimated i_N from Table S-8 calculated using the Reverse Yates Algorithm with non-significant (S = "No") variables or combinations of variables determined from the ANOVA calculation of Table S-6 set to zero during the calculation.

[b] Average of the measured i_N from Table S-4 listed in reverse order per the requirement for the reverse Yates' Algorithm calculation.

[c] Residual i_N value calculated as the difference between the average measured i_N value and the i_N value estimated from the system model using the Reverse Yates' Algorithm.

Table S-10: Information for Residuals Plot

Order (j)	Probability $P_j{}^a$	Ordered Residuals Δi_N (nA)[b]
1	1.5625	−44.5208
2	4.6875	−38.4792
3	7.8125	−30.1293
4	10.9375	−24.9792
5	14.0625	−23.921
6	17.1875	−22.8539
7	20.3125	−16.8542
8	23.4375	−16.246
9	26.5625	−15.1875
10	29.6875	−14.4627
11	32.8125	−14.3956
12	35.9375	−9.81226
13	39.0625	−8.6458
14	42.1875	−7.8542
15	45.3125	−4.47918
16	48.4375	−3.39564
17	51.5625	0.145844
18	54.6875	5.562719
19	57.8125	5.812469
20	60.9375	6.479427
21	64.0625	12.22939
22	67.1875	13.4123
23	70.3125	13.47918
24	73.4375	16.9623
25	76.5625	19.52082
26	79.6875	24.85416
27	82.8125	26.18774
28	85.9375	26.75399
29	89.0625	27.02082
30	92.1875	27.62897
31	95.3125	29.47918
32	98.4375	40.68753

[a] Cumulative probability of occurrence as defined by $P_j = 100(j − ½)/32$.
[b] Residuals from column 3 of Table S-9 ordered from smallest to largest value.

Table S-11: Photocurrent Data at Intermediate (P) Levels for Various Electrolytes

Row	Variable Levels[a]					i_P (nA)[b]			i_B (nA)[c]		
	L	F	C	P	A						
1	1	1	Cl^-	0.0117	−1	491	468	460	52	48	53
2	1	1	Cl^-	0.0117	0.5000	418	400	386	95	94	94
3	1	1	Cl^-	0.0117	1	358	343	339	87	85	83
4	1	1	ClO_4^-	0.0117	−1	407	393	387	39	46	48
5	1	1	ClO_4^-	0.0117	0.5000	296	298	294	57	63	68
6	1	1	ClO_4^-	0.0117	1	218	207	217	79	81	81
7	1	1	Br^-	0.0117	−1	440	436	417	8	8	14
8	1	1	Br^-	0.0117	0.5000	406	390	377	106	124	125
9	1	1	Br^-	0.0117	1	344	332	323	113	114	114
10	1	−1	NO_3^-	0.0117	−1	450	436	424	52	69	64
11	1	−1	NO_3^-	0.0117	0.5000	390	379	373	165	182	185
12	1	−1	NO_3^-	0.0117	1	277	270	264	132	132	139

[a] As shown in Table 2 in main article text.
[b] Measured cell photocurrent for solution containing $NaBPh_4$.
[c] Measured cell photocurrent for blank solution containing no $NaBPh_4$.

Table S-12: Photocurrent Calculations at Intermediate (P) Levels for Various Electrolytes

Row	i_N (nA) Ave.[a]	$SV(i_N)$[b]	i_P (nA) Ave.[c]	$SV(i_P)$[d]	i_B (nA) Ave.[e]	$SV(i_B)$[f]	$Cov(i_P, i_B)$[g]
1	422	261.3333	473	259	51	7	2.333333
2	307	246.5556	401.3333	257.3333	94.33333	0.333333	5.555556
3	261.6667	79	346.6667	100.3333	85	4	12.66667
4	351.3333	192.1111	395.6667	105.3333	44.33333	22.33333	−32.2222
5	233.3333	41	296	4	62.66667	30.33333	−3.33333
6	133.6667	43.66667	214	37	80.33333	1.333333	−2.66667
7	421	219	431	151	10	12	−28
8	272.6667	514.6667	391	211	118.3333	114.3333	−94.6667
9	219.3333	118.6667	333	111	113.6667	0.333333	−3.66667
10	375	354.5556	436.6667	169.3333	61.66667	76.33333	−54.4444
11	203.3333	311.7778	380.6667	74.33333	177.3333	116.3333	−60.5556
12	136	88.22222	270.3333	42.33333	134.3333	16.33333	−14.7778

[a] As shown in Table 2 in main article text. Average i_N calculated as: $i_N(Ave) = i_P(Ave) - i_B(Ave)$.
[b] Sample variance of the i_N.
[c] Average i_P calculated from individual i_P values in the corresponding row of Table S-11.
[d] Sample variance of the i_P.
[e] Average i_B calculated from individual i_B values in the corresponding row of Table S-11.
[f] Sample variance of the i_B.
[g] Sample covariance for the paired i_P, i_B measurements.